Monthly Notices of the ROYAL ASTRONOMICAL SOCIETY

MNRAS **530,** 4300–4316 (2024)
Advance Access publication 2024 April 27

https://doi.org/10.1093/mnras/stae1124

Potential climates and habitability on Gl 514 b: a super-Earth exoplanet with high eccentricity

L. Biasiotti [1,2]★ P. Simonetti [2] G. Vladilo,[1,2] S. Ivanovski,[1,2] M. Damasso,[3] A. Sozzetti [3] and S. Monai[2]

[1]*Department of Physics, University of Trieste, Via G. B. Tiepolo 11, I-34143 Trieste, Italy*
[2]*INAF - Osservatorio Astronomico di Trieste, Via G. B. Tiepolo 11, I-34143 Trieste, Italy*
[3]*INAF - Osservatorio Astrofisico di Torino, Via Osservatorio 20, I-10025 Pino Torinese, Italy*

Accepted 2024 April 23. Received 2024 April 22; in original form 2024 February 24

ABSTRACT

The recently discovered super-Earth Gl 514 b, orbiting a nearby M0.5-1.0 star at 7.6 pc, is one of the best benchmark exoplanets for understanding the potential climate states of eccentric planets. The elongated ($e = 0.45^{+0.15}_{-0.14}$) orbit of Gl 514 b, which only partially lies in the Conservative Habitable Zone, suggests a dynamically young system, where the spin-orbit tidal synchronization may not have yet occurred up to the present time. In the present work, we use a seasonal-latitudinal energy balance model, EOS-ESTM, to explore the potential impact of both constrained and unconstrained planetary, orbital, and atmospheric parameters on the Gl 514 b habitability, mapped in terms of surface temperature. We test three distinct CO_2-dominated atmospheres by varying the CH_4 concentration values (0 per cent, 0.1 per cent, and 1 per cent) and the total surface pressure. As a general trend, we find that habitable conditions are favoured by high-CH_4 and high-pressure regimes. Habitability also increases for high-axis obliquities (at least until the appearance of an icebelt), long-rotation periods, and high-ocean fractional coverage. If the ocean fraction is low, then also the argument of periastron becomes relevant. Our results are robust against changes of the continental distribution. Thus, we conclude that Gl 514 b can potentially maintain temperate surface conditions with modest seasonal temperature variations under a wide variety of planetary, orbital, and atmospheric conditions. Despite no transit have been detected yet, the results found in this work should motivate the community to invest time in future observations.

Key words: astrobiology – planets and satellites: atmospheres – planets and satellites: individual: Gl 514 b – planets and satellites: terrestrial planets – stars: activity.

1 INTRODUCTION

The search for biosignatures in exoplanetary atmospheres is one of the main drivers of present-day astronomical projects. To optimize the use of state-of-the-art, space-born instrumentation, this endeavour requires a careful selection of rocky exoplanets potentially able to host life. To this end, it is essential to supplement observational data with theoretical predictions of surface planetary conditions performed with the aid of climate models.

Traditionally, habitability studies rely on the classic definition of the Conservative Habitable Zone (CHZ, Kasting, Whitmire & Reynolds 1993), and in particular on the updated calculations by Kopparapu et al. (2013). In essence, habitability is defined on the basis of the surface temperature, which must be in the liquid water range. The surface temperature is then calculated using single-column Energy Balance Models (EBMs) for a given atmospheric composition and instellation. Since this class of models deal with quantities averaged over one orbit, latitudinal and seasonal variations of temperature are neglected. More complex models, like seasonal-latitudinal EBMs or computationally intensive Global Circulation Models (GCMs) are needed to investigate a planet which is only partially habitable, either in time or space.

The recently discovered super-Earth planet Gl 514 b (Damasso et al. 2022), orbiting the nearby (d = 7.6 pc) M-dwarf, is one of the most interesting cases to investigate potential climates of planets that radically differ from the Earth. Due to the combination of its relatively large semimajor axis ($a = 0.422^{+0.014}_{-0.015}$ au) and eccentricity ($e = 0.45^{+0.15}_{-0.14}$), Gl 514 b lies part of the time inside the CHZ (about 34 per cent of the orbital period) and the rest of the time beyond the outer edge of the CHZ. The fraction of time inside the optimistic HZ (Kopparapu et al. 2013) is even higher (37.7 per cent), reinforcing the importance of Gl 514 b as a test case for a study of seasonal variations of habitability. This suggests the presence of strong seasonal variations that impact the actual habitability of the planet. Investigating the potential climates of planets that exhibit seasonal episodes of habitability can provide insights into the dynamic nature of planetary habitability and the potential for the support of life in exotic scenarios. In this sense, the study of the habitability of Gl 514 b can be generalized to all those cases in which there are strong excursions of instellation at different phases of the orbit, thus helping to define a 'Seasonal Habitable Zone'.

★ E-mail: lorenzo.biasiotti@gmail.com

In this work, we use an enhanced seasonal-latitudinal EBM featuring a treatment of the meridional energy transport calibrated with 3D models (Vladilo et al. 2015) and an upgraded treatment of surface planetary properties (Biasiotti et al. 2022), coupled with a physical description of the vertical atmospheric radiative transfer (RT; Simonetti et al. 2022). Thanks to the model computational efficiency and flexibility, we can explore the climate impact of planetary properties unconstrained by observations, treating unknown quantities as free parameters, with the goal to assess how likely is Gl 514 b to be habitable, at least in a qualitative way, and to generalize our findings to all high-eccentricity super-Earths of astrobiological interest.

This paper is structured as follows. In the next section, we discuss the observational data that are relevant for constraining the climate of Gl 514 b. In Section 3, we describe the climate models employed in our analysis. The model parametrization and predictions of climate simulations are presented in Section 4, where we explore how the surface habitability varies in different plausible scenarios of planetary and atmospheric parameters. These results are discussed in Section 5 and the conclusions and implications of this work are summarized in Section 6.

2 SUMMARY OF OBSERVATIONAL DATA

2.1 The host star Gl 514

Gl 514 has been extensively monitored since 2004 and its main properties are summarized in Table 1. Essential information on the photospheric and physical parameters have been derived in the last decade (Turnbull 2015; Stassun et al. 2019). The two most important quantities that affect the planetary energy budget and climate are the absolute luminosity, which determines the instellation of the planet, and the energy distribution of stellar photons, which affects the planetary albedo. An M-dwarf star emits a substantial portion of its radiation in the near-infrared wavelengths, a factor that profoundly influences the albedo and climate. Over 90 per cent of the radiation emitted by the M-dwarf star such as Gl 514 occurs at wavelengths longer than 0.7 μm, in contrast to nearly 53 per cent for the sun (Shields et al. 2013).

2.1.1 The age of Gl 514

The age of the star can be used to estimate the evolutionary state of the planet. Unfortunately, the age is the quantity most difficult to accurately measure in stars (Engle & Guinan 2023). Recently, Damasso et al. (2022) has provided a lower limit to the kinematical age of Gl 514, $t_\star \geq 0.8$ Gyr, considering the deviation of its space velocities from that of known young stellar moving groups.

Given the 'spin-down effect', whereby the star's rotation period lengthen as they age, it is possible to constrain the age of the star from a measurement of its rotation period. The rotation period of Gl 514 has been estimated adopting distinct methods. Analysis of the spectroscopic activity indices from HARPS spectra yield $P_{\star,\,\mathrm{rot}} = 28.0 \pm 2.9$ d (Suárez Mascareño et al. 2015). Analysis of CARMENES spectra yields 30.8 ± 0.3 d using the H_α line and 30.3 ± 0.2 d using the Ca II infrared triplet (Fuhrmeister et al. 2019). Combining 25 yr of observations with the HIRES, HARPS, and CARMENES spectrographs, Damasso et al. (2022) found $P_{\star,\,\mathrm{rot}} = 30.6 \pm 0.3$ d. From this value and the age–rotation relationship described in Engle & Guinan (2023), we derive an age of $\sim$3.0 $\pm$ 0.9 Gyr. Analysis of *TESS* photometric data yields a signal with periodicity of $\sim$2.5 d (Damasso et al. 2022; Fetherolf et al. 2023) that could be interpreted either as a transit or as a modulation due to stellar rotation. However, the low-signal detection efficiency ($\sim$3.9) found by Damasso et al. (2022), and the high value reduced χ^2 ($\sim$2.8) reported in the *TESS* stellar variability catalogue (Fetherolf et al. 2023) do not support any of these two interpretations.

Also the level of stellar activity is age-dependent since the stellar magnetic field responsible for the activity decreases with time as the star spins down. In this context, an important age estimator for main-sequence stars is the R'_{HK} index, which measures the chromospheric emission in the cores of the broad photospheric Ca II H and K absorption lines (Mamajek & Hillenbrand 2008). Recently, Astudillo-Defru et al. (2017a) measured the R'_{HK} of 403 M-dwarfs of the HARPS sample and derived $R'_{\mathrm{HK}} = -4.879$ for Gl 514. A similar result was found by Marvin et al. (2023), despite using different methods to measure R'_{HK} in M dwarfs. Several attempts to establish an R'_{HK}–age relation have been performed (e.g. Barry, Cromwell & Hege 1987; Soderblom, Duncan & Johnson 1991; Lachaume et al. 1999). Reviewing these works, Mamajek & Hillenbrand (2008) assembled R'_{HK} data from the literature for young stellar clusters and provided an updated relation (see equation 3 therein), which returns $t_* \sim 3.5 \pm 1.2$ Gyr for Gl 514. This value is in accordance with the value derived from the age–rotation relationship.

Table 1. Upper: coordinates, spectral classification, and photospheric, physical parameters of Gl 514. Lower: planetary parameters of Gl 514 b.

Stellar parameters	Value	Reference
Spectral type	M0.5-M1.0 V	1
	M1.0 V	2
	M0.5 V	4
Distance, d (pc)	7.617780 ± 0.003175	1
Effective temperature, T_{eff} (K)	3728 ± 68	1
	3707	2
	3697.0 ± 157.0	3
Metallicity, [Fe/H] (dex)	-0.14 ± 0.09	1
Rotation period, $P_{\star,\,\mathrm{rot}}$ (days)	30.6 ± 0.3	1
	28.0 ± 2.9	5
	30.3 ± 0.2	6
	30.8 ± 0.3	6
Luminosity, L_* (log10($L_\odot$))	$-1.4^{+0.1}_{-0.1}$	1
	$-1.398^{+0.512}_{-0.097}$	2
	$-1.37119^{+0.09039}_{-0.11429}$	3
Mass, M_* ($M_\odot$)	0.510 ± 0.051	1
	0.45	2
	0.5007770 ± 0.0204632	3
Radius, R_* ($R_\odot$)	0.500 ± 0.047	1
	0.51	2
	0.5027600 ± 0.0151819	3
Age, t_* (Gyr)	>0.8	1
Chromospheric activity, log(R'_{HK})	-4.86 (T_{eff}, SpT)	9
	-4.82 (T_{eff}, M_*)	9
	-4.88	10
Planetary parameters		
Averaged semimajor axis, $\overline{a}$ (au)	$0.422^{+0.014}_{-0.015}$	1
Averaged instellation, $\overline{S}$ (S_0)	$0.28^{+0.06}_{-0.05}$	1
Eccentricity, e	$0.45^{+0.15}_{-0.14}$	1
Orbital period, P (days)	140.43 ± 0.41	1
Minimum mass, $m_p \sin i$ ($M_\oplus$)	5.2 ± 0.9	1

References: 1. Damasso et al. (2022); 2. Turnbull (2015); 3. Stassun et al. (2019), 4. Hawley, Gizis & Reid (1996), 5. Suárez Mascareño et al. (2015); 6. Fuhrmeister et al. (2019); 7. Gaia Collaboration (2021); 8. Bailer-Jones et al. (2018); 9. Marvin et al. (2023); 10. Astudillo-Defru et al. (2017a).

2.2 The planet Gl 514 b

The analysis of the radial-velocity data collected over 25 yr indicates that Gl 514 b has a minimum mass $M_p \sin i = 5.2 \pm 0.9\,M_\oplus$ (Damasso et al. 2022). To date, no transits of Gl 514 b have been detected. A search for transit-like signals in the light curves observed by *TESS* (Ricker, Winn & Vanderspek 2015) has given negative results (Damasso et al. 2022). Despite the lack of radius measurement, the chance that Gl 514 b is a rocky super-Earth is high, with a posterior transit probability of 0.63 per cent.[1] Indeed, the probability that the orbital inclination i lies between 30° and 90° is $\simeq 87$ per cent (Fischer et al. 2014), meaning that the mass lies within a factor of 2 of the minimum mass, posing Gl 514 b as a super-Earth (Valencia, O'Connell & Sasselov 2006). Assuming an internal composition similar to that of the Earth (25 per cent of Fe and 75 per cent of rock) we can estimate the radius, R_P, and the gravity, g, that are required for the climate calculations, by means of a mass–radius relationship derived from statistical studies of exoplanets. By inserting $M_p = 5.2\,M_\oplus$ in the relation derived by Fortney, Marley & Barnes (2007), we obtain $R_p = 1.57\,R_\oplus$ and $g = 2.1\,g_\oplus$. Luckily, climate models are robust against small variations in R_p and g (see Section 3). This fact provides confidence in the overall predictive analysis performed in this work.

2.2.1 *The orbital eccentricity*

Several studies have investigated the critical role of eccentricity on exoplanets' climates and habitability (e.g. Williams & Pollard 2002; Dressing et al. 2010; Linsenmeier, Pascale & Lucarini 2015; Wang et al. 2017; Way & Georgakarakos 2017; Kane et al. 2021; Damasso et al. 2022). These works generally agree on assuming such worlds habitable, despite the dramatic seasonal changes in the instellation between the periastron and the apoastron. However, they concur that planets located near the outer regions of the habitable zone may enter a globally frozen 'snowball' state, posing a threat to their ability to support water-based life (Dressing et al. 2010). Detailed climate studies of highly eccentric planets provide a means for testing these predictions. In this context, Gl 514 b offers the best chance for such investigations. In fact, among the confirmed exoplanets orbiting around M-dwarfs, only two super-Earths may have an eccentricity as high as Gl 514 b: Wolf 1061 d ($e = 0.55^{+0.08}_{-0.09}$, Astudillo-Defru et al. 2017b) and, possibly, TOI-1470 c (e <0.50, González-Álvarez et al. 2023) (see Fig. 1). Gl 514 b periodically traverses the conservative HZ, residing within this zone for nearly 34 per cent of its orbital period (see fig. 16 in Damasso et al. 2022). The elongated orbit of Gl 514 b induces an instellation about 7 times stronger at the periastron (0.611 au) than at the apoastron (0.231 au). Since the planet moves slower near the apoastron than near the periastron, the winter/summer season around the apoastron can be considerably longer than the summer/winter season around the periastron. Whether these dramatic changes in instellation may cause extreme seasonal variations is discussed in Section 4.

2.2.2 *Long term evolution of planetary properties*

The luminosity of the star as well as the boundaries of its CHZ change during its lifetime. The shaded area in light-blue in Fig. 2 shows the temporal variation of the boundaries of the CHZ, computed adopting the evolutionary model for a star with a mass of $0.5\,M_\odot$, similar to Gl 514 (Baraffe et al. 1998). The red bar, plotted for a putative age of ∼3 Gyr, represents the present-day excursion between periastron and apoastron, the latter lying well beyond the outer edge of the CHZ. Assuming a modest evolution of the orbital parameters, one can see that in the early stages after planetary formation the planet was predominantly in habitable conditions for a period of a few 10^7 yr. This encourages us to explore to which extent the habitability may persist up to the present time.

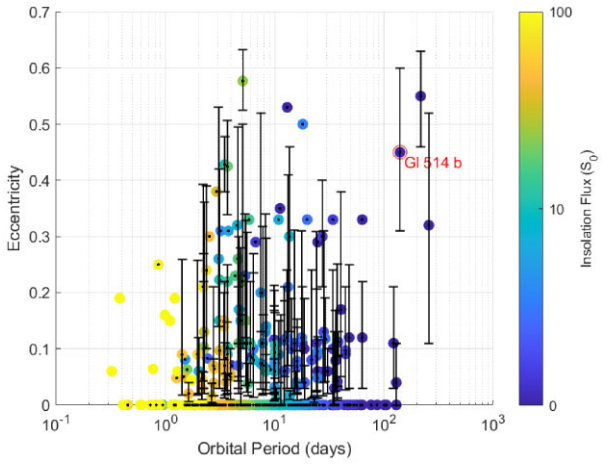

Figure 1. Eccentricity versus orbital period for the confirmed exoplanets orbiting around M-type stars. The red dot shows the position of Gl 514 b. The instellation flux of each planet is highlighted by a colourbar. Horizontal lines indicate the mass of Solar system giant planets.

Besides the instellation, also the orbital eccentricity and planet rotation period vary with time as a result of the tidal interactions with the central star. The high orbital eccentricity of Gl 514 b suggests that the system is dynamically young. However, it is hard to constrain the age from this argument, because orbital circularization around low-mass stars is predicted to take place in time-scales that range from a few 10^8 up to a few 10^9 yr, depending not only on the stellar and planetary parameters, but also on the type of model adopted (Barnes 2017). In any case, the high eccentricity suggests that the age of the system might be closer to the lower bounds of the estimates of $t_\star$.

For the purpose of the climate modellization it is important to understand whether or not Gl 514 b is tidally locked as a result of the rotational spin-down. To test if the planet lies within the tidal lock limit, r_τ, we adopted the formula (Peale 1977)

$$r_\tau \propto K\, R_P^{1/2}\, M_P^{-1/6}\, P_{\rm rot,init}^{1/6}\, M_\star^{1/3}\, t_\star^{1/6}, \quad (1)$$

where the coefficient K depends on the tidal parameters of Gl 514 b, such as the dissipation function of the planet, Q, and the tidal Love number, k_2. Accurate determination of these parameters, taking into account the internal planetary structure, is fundamental to characterize the rotational and orbital history (Tobie et al. 2019). In the present work, we adopt two values of k_2/Q that provide a sort of lower and upper limit for r_τ. One is based on the most accurate measurement derived for the Moon (Dickey et al. 1994), i.e. $k_2/Q = 0.001136 \pm 0.000016$. For the other one we adopt the dissipation function (Tobie et al. 2019)

$$Q = 10^{(A+B\alpha)} \times \left(\frac{\chi\,\eta}{\chi_{\rm ref}\,\eta_{\rm ref}}\right)^{\alpha}, \quad (2)$$

[1]This value has been calculated adopting the formulation given by Stevens & Gaudi (2013) and it is very similar to the geometrical transit probability of 0.5 per cent (Damasso & Nardiello 2022; Damasso et al. 2022).

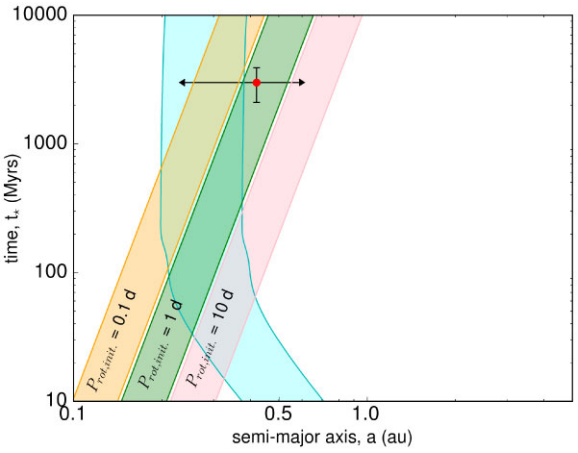

Figure 2. Shaded area in light blue: temporal evolution of conservative HZ limits (Kopparapu et al. 2013) obtained from the stellar evolutionary tracks of Baraffe et al. (1998). The horizontal arrow shows the apoastron and periastron of Gl 514 b for a putative age of ∼3 Gyr, whose errors are delimited by the vertical bar. The other shaded areas indicate the tidal lock limit assuming three distinct initial rotation periods for the planet: $P_{\rm rot,\,init} = 0.1$ (orange), 1 (green), and 10 (pink) d (see Table 2).

Table 2. Tidal lock radius, r_τ, calculated with equation (1) for $t_\star = 3$ Gyrs. First row: results obtained for $k_2/Q = 0.0011$, similar to that derived for the Moon (Dickey et al. 1994). Second row: results obtained for Q and k_2 values specific for a super-Earth (see subsection 2.2.2).

	k_2/Q	$P_{\rm rot,\,init}$ (d)		
		0.1	1	10
r_τ (au)	0.0011	0.26	0.38	0.55
r_τ (au)	0.0050	0.37	0.54	0.79

where the coefficients A and B depend on the iron content, $\delta_{\rm Fe}$.[2], $\eta_{\rm ref}$ is the reference value for the viscosity profile ($\eta_{\rm ref} = 2\pi/1$ d), and $\chi_{\rm ref} = 5 \times 10^{22}$ Pa s is a reference viscosity in the high-pressure silicate mantle layer, where $\alpha = 0.3$. For $\eta\chi$ in the range 10^{16}–10^{18} Pa, typical of a rocky super-Earth, Q varies from 90 to 360, well above the Earth value (Q ∼12, Murray & Dermott 1999). These higher values of dissipation factor are appropriate for super-Earths because the rigidity increases due to self-gravitation, suppressing tidal bulges (Efroimsky 2012). Following a similar approach, we estimate k_2 as a function of the planetary mass and iron content adopting the parametrization (Tobie et al. 2019)

$$k_2(\delta_{\rm Fe}) = k_2^{1M_\oplus}(\delta_{\rm Fe}) - \left[\frac{1-\left(\frac{g}{g_\oplus}\right)^2}{1+\left(\frac{g}{g_\oplus}\right)^2}\right] \times \Delta k_2(\delta_{\rm Fe}), \quad (3)$$

where $k_2^{1M_\oplus}$ is the k_2 value for a mass equal to that of the Earth and Δk_2 is the correction required to obtain k_2 for masses ranges from 0.1 to 10 $M_\oplus$. These coefficients can be estimated as a function of iron content using a polynomial fit provided by Tobie et al. (2019). In this way, adopting $g = 2.1\,g_\oplus$ for Gl 514 b, we obtain $k_2 = 0.45$ which, combined with $Q = 90$, yields k_2/Q=0.005.

[2]We assume an internal composition similar to that of the Earth, $\delta_{\rm Fe} = 25$ per cent.

Fig. 2 shows how the tidal lock radius, r_τ, calculated at $t_\star = 3$ Gyr compares with the planet position ($a = 0.42$ au), depending on the initial rotation period, $P_{\rm rot,\,init}$, and the adopted value of k_2/Q. Since Gl 514 b is more massive than the Earth, it may have accumulated a larger angular momentum, $L \propto MR^2 w$, at the stage of its accretion, starting its dynamical evolution with a fast rotation[3] Assuming $P_{\rm rot,\,init}$ = 0.1 d, Gl 514 b would become tidally locked only after 5 Gyr. We conclude that spin-orbit tidal synchronization did not take place for most of the planet's life, and perhaps may not have yet occurred up to the present time. For this reason, and due to limitations of the validity of our code, Earth-like planets Surface Temperature Model (ESTM), at very short and long rotation periods (Vladilo et al. 2015; Biasiotti et al. 2022), here we consider rotation periods in the interval 0.5–10 d to explore the potential climates of Gl 514 b (see further section). It is worth recalling that zonally averaged models, as ESTM, cannot be applied to tidally locked planets that always expose the same face to their host stars.

Finally, it is worth mentioning that also stellar encounters may play a role in the long term dynamical evolution of the planet orbital parameters. As a matter of fact, in the case of the Solar system, chaotic diffusion of rocky planets can be triggered by the perturbations that stellar passages impart on the orbits of giant planets (Kaib & Raymond 2024). Modelling these perturbations in the case of Gl 514 b is beyond the scope of the present work.

3 METHODS

The aim of the this Paper is to derive the surface temperature (T) of Gl 514 b in order to calculate two indexes of partial habitability, h and h_c, detailed in Vladilo et al. (2015) and briefly described in subsection 3.3. Apart from the minimum mass of the planet and some of its orbital elements (a and e), no other data is currently available about this object. Moreover, e is subject to a relatively large error, at least with respect to its potential impact on the planet's climate. As such, studying the climate of Gl 514 b is only possible by treating a variety of fundamental but completely unknown planetary (e.g. axis obliquity, rotation period) and atmospheric (e.g. surface pressure, chemical composition) features as free parameters and by performing a parameter space exploration. Further, we detail the coupled RT and climate model employed in this work and the specific parametrizations concerning the surface and cloud properties adopted.

3.1 The ESTM model

The ESTM is a seasonal-latitudinal EBM with enhanced parametrizations of the horizontal heat diffusion, the cloud radiative properties and ice coverage growth. At its core, ESTM integrates the diffusion equation of energy balance (e.g. North & Coakley 1979; North, Short & Mengel 1983; Williams & Kasting 1997; Spiegel, Menou & Scharf 2008)

$$\mathcal{C}\frac{\partial T}{\partial t} - \frac{\partial}{\partial x}\left[\mathcal{D}\,(1-x^2)\,\frac{\partial T}{\partial x}\right] + \mathcal{O} = \mathcal{S}\,(1-\mathcal{A}), \quad (4)$$

where $x = \sin\varphi$. The model converges to a limit cycle after a number of orbits, giving as output a map of T as a function of the latitude φ and the orbital phase t. Longitudinal variability is neglected and $T(\varphi)$ is averaged over one rotation period. We summarize each term of the equation starting from the left side

[3]Giant planets in the Solar system have a fast rotation period.

(i) the term $\mathcal{C}$ represents the zonal heat capacity. In this work we consider three type of surfaces, namely land, ocean and ice, all of which contribute to the final thermal capacity at each latitude by their cover fraction. As far as the thermal impact of the oceans, in line with previous climate studies performed with EBMs, we account for the short-term thermal impact of oceans by considering the contribution of the mixed layer. Specifically, we adopt a mixed-layer contribution ($C_{\rm ml}$) equivalent to the thermal inertia of a 50-m wind-mixed ocean layer (Biasiotti et al. 2022).

(ii) The diffusion term $\mathcal{D}$ describes the meridional heat transport, which is treated as purely diffusive

$$\Phi \equiv -\mathcal{D}\frac{\partial T}{\partial \varphi}, \tag{5}$$

where $2\pi R^2 \Phi \cos\varphi$ is the net rate of atmospheric heat transport across a circle of constant latitude and R is the planet radius. In ESTM, $\mathcal{D}$ is a function of the planetary radius and rotational period, the surface pressure and gravity, the mean molecular weight, and the absolute humidity. The enhanced efficiency associated with a Hadley cell-like circulation is taken into consideration, as it is the displacement of the thermal equator in planets with non-zero obliquities.
We refer the reader to (Vladilo et al. 2015) for a detailed description of the physics behind this formalism;

(iii) The Outgoing Longwave Radiation ($\mathcal{O}$) represents the thermal radiation emitted to space at each latitude as a function of T. In our model, $\mathcal{O}$ is calculated for a specified set of atmospheric properties (chemical composition, surface pressure, vertical pressure–temperature profile) and for a grid of T values by EOS, saved in a look-up table and interpolated during calculations by ESTM;

(iv) $\mathcal{S}$ is the instellation, calculated in a set of specified points of the orbit. In this work, we integrate equation (4) on 24 points.

(v) The term $\mathcal{A}$ is the planetary albedo at the top of the atmosphere. As for $\mathcal{O}$, ESTM interpolates $\mathcal{A}$ from look-up tables, pre-calculated by EOS on a grid of T, stellar zenith angles z and surface albedos $a_{\rm srf}$. The albedo of clouds is taken into account separately via a simplified parametrization.

The ESTM code has been extensively calibrated and validated using both Earth data (Biasiotti et al. 2022) and the results of sophisticated 3D GCMs (Vladilo et al. 2015). It has already been employed to study the habitability of Kepler-452b (Silva et al. 2017), the Snowball-Temperate climate bistability (Murante et al. 2020) and the climate of the Early Mars (Simonetti et al. 2024). It is also a participant of the Functionality of Ice Line Latitudinal EBM Tenacity (FILLET) Intercomparison Project (Deitrick et al. 2023). Finally, it is worth mentioning that zonally averaged models, as ESTM, cannot be applied to tidally locked planets that always expose the same face to their host stars (Vladilo et al. 2015).

3.2 The EOS model

EOS (Simonetti et al. 2022) is a RT model derived from the GPU-accelerated codes HELIOS (Malik et al. 2019) and HELIOS-K (Grimm et al. 2021) which has been validated against other standard RT suites for a wide range of atmospheric chemical compositions. It operates in the two-stream approximation and includes prescriptions for non-isotropic scattering. RT calculations can be carried on either line-by-line or using k-distribution opacities. EOS can be operated both 'forward', i.e. by specifying $\mathcal{S}$ and retrieving a vertical atmospheric pressure–temperature profile and a T value, or 'backward', that is, by imposing a profile and a T and obtaining a $\mathcal{O}$ and a reflectance values as a result. The $\mathcal{S}$ needed to sustain the initially specified T can then be obtained by considering the energy balance equation for a single atmospheric column: $\mathcal{O} = \mathcal{S}\,(1 - \mathcal{A})$.

In this work, we employed EOS to calculate the RT look-up tables for our seasonal-latitudinal EBM via the 'backward' method (Kasting et al. 1993, as e.g. in). $\mathcal{O}$ has been calculated on an evenly spaced grid in T in the [160, 360] K interval, with a 5 K step, for each total dry surface pressure $p_{\rm tot}$ in the {1.0, 2.0, 4.0, 6.0, 8.0, 10.0, 12.8, 16.7, 22.0} bar set. For T corresponding to $p_{\rm tot}$ higher than the condensation pressure of the main atmospheric gas, CO_2, the condensation pressure has been used instead. $\mathcal{A}$ has been calculated for the same $p_{\rm tot}$ and T interval, but using a 20 K step. As for the two other quantities (z and $a_{\rm srf}$) $\mathcal{A}$ depends upon, we adopted the $\{0, 45, 60, 70, 75, 80, 83, 85, 88\}^\circ$ and {0.0, 0.15, 0.30, 0.6, 0.9} grids, respectively. We used the spectral-line lists available on HITRAN2020 (Gordon et al. 2022) for three gases: CO_2, H_2O, and CH_4. The reasons for these choices are discussed in subsection 3.4. The CO_2 absorption lines are modelled following Perrin & Hartmann (1989) and the wings are truncated at 500 cm^{-1} from the line centre, while the H_2O and CH_4 absorption lines are considered Voigtian and truncated at 25 cm^{-1}. We also included the CO_2–CO_2 Collision-Induced Absorptions (CIAs) in the 0–750 cm^{-1} (Gruszka & Borysow 1997, 1998) and 1000–1800 cm^{-1} (Baranov & Vigasin 1999) ranges and the CO_2-CH_4 CIAs in the 0–2000 cm^{-1} range (Wordsworth et al. 2017). Self- and foreign-induced CIAs for H_2O have instead been calculated using the MT_CKD v3.4 (Clough, Kneizys & Davies 1989; Mlawer et al. 2012) model. All the considered species contribute to the atmospheric reflectance via Rayleigh scattering (Sneep & Ubachs 2005; Wagner & Kretzschmar 2008). Concerning the vertical structure of the atmosphere, we adopted two saturated moist pseudo-adiabatic profiles for the lower and upper troposphere, where H_2O and CO_2 condensation can respectively occur, and a 155 K isothermal stratosphere. The atmosphere is divided in a number of log-spaced layers, adjusted in order to maintain a constant layer density of 10 per order-of-magnitude in pressure. The uppermost layer is always at 10^{-5} bar.

3.3 The habitability indexes h and h_c

For the purpose of this investigation, we derive the fractional habitability index, h, from the latitudinal and seasonal variations of surface temperature, $T(t, \varphi)$, by adopting the liquid-water temperature thresholds, $T_{\rm ice}$ and $T_{\rm boil}$, representative of the thermal limits of a habitable environment. The former refers to the lower limit for the presence of liquid water, that is, 273.15 K, whereas $T_{\rm vapour} = T_{\rm boil}(p_{\rm tot})$ is the water boiling point, which depends on the surface pressure. In practice, we calculate the mean fraction of planet surface that is habitable during the orbital period using the relation (Vladilo et al. 2013; Jansen et al. 2019)

$$h = \frac{\int_{-\pi/2}^{\pi/2} d\varphi \int_0^{P_{rot}} dt [H(t,\varphi)\cos\varphi]}{2P_{rot}}, \tag{6}$$

where $H(t, \varphi)$ is the habitability function, which is defined as a boxcar function, such that $H(t, \varphi) \equiv 1$ when $T(t, \varphi) \in (T_{\rm ice}, T_{\rm boil})$ and $H(t, \varphi) \equiv 0$ when $T(t, \varphi) \notin (T_{\rm ice}, T_{\rm boil})$. In addition to h, we also calculate the continuous habitability index, h_c, by summing the fractional areas of the latitude zones that are continuously habitable during the whole orbital period (see Vladilo et al. 2013). By construction, $h_c = 0$ if all the latitude zones undergo a period of non-habitability during the orbital revolution.

3.4 Atmospheric parameters

Since Gl 514 b receives a lower instellation than Earth, we model its atmosphere as CO_2-dominated, following the long-standing argument that, on planets colder than Earth, CO_2 tends to accumulate due to inefficient removal by silicate weathering (Walker, Hays & Kasting 1981). CO_2 is one of the main components of degassed fluids on Earth (e.g. Giggenbach 1996) and likely on other planets (Gaillard & Scaillet 2014) and it is relatively stable against photolysis and non-hydrodynamic atmospheric escape due to its relatively high-molecular weight. As such, it is a good candidate as the main greenhouse contributor in exoplanets near the outer edge of the CHZ (Kasting et al. 1993). We also include H_2O by setting a constant relative humidity (*RH*) everywhere in the troposphere of 100 per cent. This value is higher than the average *RH* of Earth (60 per cent, see e.g. fig. 2 in Brun et al. 2022) but it is usually assumed in the calculation of the outer edge of the CHZ (Kopparapu et al. 2013), thus simplifying the comparison between our results and the literature.

Methane is another important gas that might significantly contribute to the habitability of super Earths (Ramirez & Kaltenegger 2018), although its effectiveness depends strongly on the Spectral Energy Distribution (SED) of the incoming stellar light. At variance with other reduced species that can enhance the greenhouse effect on a rocky exoplanet (Sagan & Chyba 1997), CH_4 is the only one that we empirically observe in high concentrations, namely in the atmosphere of Titan (Catling & Kasting 2017). CH_4 can be produced by the serpentinization of mafic and ultramafic rocks by water (Chassefière et al. 2013) and can potentially be maintained at the percent concentration level even if this process happens over a small fraction of the planetary surface (Ramirez & Kaltenegger 2018). There is evidence that serpentinization happens also in very dry environments, such as the present-day Mars (Etiope, Ehlmann & Schoell 2013), thus it is reasonable to assume it can take place on Gl 514 b. Alternatively, at relatively high concentrations ($\sim$10 per cent) the formation of antigreenhouse, reflective organic hazes is expected to happen (Trainer et al. 2006). As such, for this work we limit ourselves to modestly CH_4-enriched cases, that are more likely to occur and easier to model with EOS. In particular, we tested atmospheres with three CH_4 concentration values x_{CH4}: 0 per cent, 0.1 per cent, and 1 per cent.

The interval of pressures that we decided to investigate is instead dictated by the maximum greenhouse limit for a CO_2-dominated atmosphere. CO_2 is an efficient Rayleigh scatterer, which causes $\mathcal{A}$ to increase as a function of $p_{\rm tot}$. Above a given surface pressure threshold $p_{\rm thr}$, this becomes dominant over the greenhouse effect and further additions of CO_2 cool, rather than warm, the planet. For Gl 514 b and the case with $x_{\rm CH4} = 0$ per cent, $p_{\rm thr}$ $\sim$17 bar if $a_{\rm srf} = 0.2$, or $\sim$23 bar if $a_{\rm srf} = 0.38$. Another issue that may arise at high enough $p_{\rm tot}$ is the condensation of CO_2 at surface. At 273 K, the condensation pressure of CO_2 is 34.7 bar. In order to avoid the complications related to the presence of a dual liquid reservoir (i.e. water and CO_2) on the surface, we limit ourselves to pressures below 13 bars.

3.5 Surface properties

EOS-ESTM calculates the value of $a_{\rm srf}$ at each latitudinal zone by averaging the albedo of each of the four types of surfaces treated by the model (i.e. land, ocean, marine ice, and land ice) in that zone, properly weighted according to their fractional coverage. Since $a_{\rm srf}$ depends on SED of the star, we cannot use the values derived in Biasiotti et al. (2022) for the Earth–Sun system. Instead, we adopt the results of Shields et al. (2013)[4], who calculated the theoretical reflectances of several type of planetary surfaces illuminated by the M3-type star AD Leo, which has a spectral distribution similar to that of Gl 514. Specifically, we adopt a land albedo a_l equal to 0.38 (see Table 3), which refers to a bare, desert-like surface, an albedo of ice over lands $a_{\rm il}$ equal to 0.5, which refers to a surface totally covered by snow, and an albedo of ice over oceans $a_{\rm io}$ equal to 0.35, that corresponds to a mixture of 62 per cent of blue marine ice and 38 per cent of snow.

Table 3. Grid of parameters adopted for the simulations. The derived values of planetary albedo are associated to the mean annual value of $\mu = \cos Z = 0.5$, where $Z = 60^\circ$.

Albedo parameters	Value	Reference
Land albedo, $a_{\rm l}$ (bare land)	0.38	1
Ice over land albedo, $a_{\rm il}$ (snow)	0.52	1
Ice over ocean albedo, $a_{\rm io}$ (mixture of 60 per cent snow and 40 per cent blue marine ice)	0.35	1
Cloud albedo, $a_{\rm c}$	0.40	2

References: 1. Shields et al. (2013); 2. Ding et al. (2021); 3. Biasiotti et al. (2022).

The albedo of the oceans (a_o) plays an especially important role due to our choice of treating the planet as having a high (0.75) fraction of the surface covered by water. While planetary habitability seems not to strictly require such a high water content, and the biosphere lifetime might even be longer on planets with a smaller surface water reservoir (e.g. Abe et al. 2011; Zsom et al. 2013), we see no particular reason against choosing an Earth-like value for Gl 514 b. Shields et al. (2013) (see fig. 1 therein) shows that the effect of the host star SED on the albedo of oceans is negligible. Therefore, we stick to the parametrization described in Biasiotti et al. (2022), which is taken from Enomoto (2007). All the surface albedos depends of z.

As far as the ice fractional coverage is concerned, we stick to the prescriptions specified in Biasiotti et al. (2022). The ice cover increases when T decrease following a generalized logistic function calibrated on Earth data and separately for lands and oceans.

3.6 Cloud properties

The significance of clouds in the thermal equilibrium of a planet poses a critical challenge for classic EBMs, since no explicit fluid dynamics calculation is carried out. As such, no microphysical properties of clouds can be actually replicated using EBMs, that are instead limited to simplified parametrizations of their spatial distribution and bulk radiative impact on the zonal energy balance. EOS-ESTM adopts a similar approach by modelling clouds in terms of fractional coverage f_c, which in turn depends on the type of underlying surface, albedo a_c and OLR forcing *CRE*.

More specifically, we assume that a_c depends on (i) the mean stellar zenith distance of the latitude zone of interest and (ii) the albedo of the underlying surface. The latter dependence is captured by considering the shortwave transmittance coefficient t, that is, the fraction of radiation not absorbed between the cloud top and the surface. The t and *CRE* parameters scale with T in order to take into

[4]We refer to the broad-band planetary albedos indicated in Table 2 and calculated without including Rayleigh scattering, atmospheric gas absorption, and clouds.

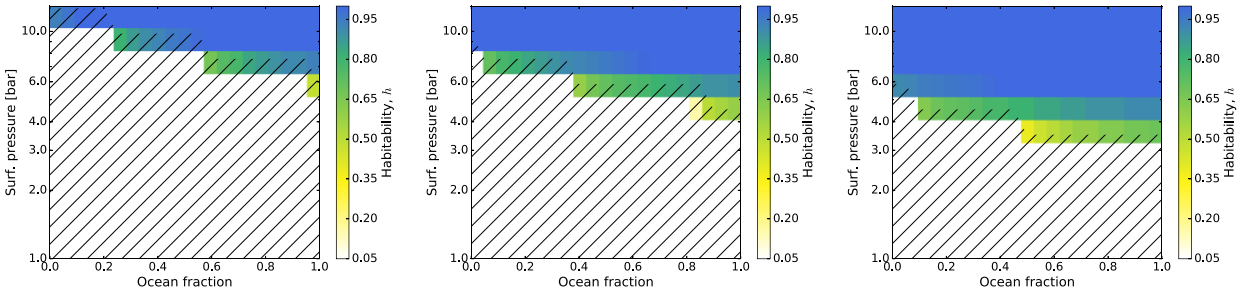

Figure 3. Predicted values of the habitability index, h, as a function of the ocean cover fraction and total surface pressure for three different atmospheric compositions. Left panel: CO_2-dominated; middle panel: CO_2+0.1 per cent CH_4; right panel: CO_2+1 per cent CH_4. For the remaining parameters we adopt $\epsilon = 23.44°$, $P_{\rm rot} = 1$ d and $\omega_{\rm peri} = 0°$. The dashed areas indicate the parameter space in which atmospheric CO_2 condensates.

consideration, albeit in a simplified way, the different properties of thick intertropical and thin polar clouds.

The values and dependences of t, *CRE*, and the cloud cover fractions over land, ocean and ice are kept equal to those presented in tables 7 and 8 in Biasiotti et al. (2022). On the other hand, we adjusted a_c in order to take into consideration the difference in the SEDs of the sun and Gl 514 by means of the following procedure.

First, we convolved the SED of both the sun and Gl 514 with the average spectral reflectance of the Earth clouds[5] The spectral reflectance of clouds was taken from existing literature. In particular, we consider the data published by Ding et al. (2021), who computed the overall reflection spectrum of Earth clouds without distinguishing between high-, mid-, and low-altitude ones (as happens in EOS-ESTM). Secondly, we compared the two results, finding that Earth-like clouds are ∼10 per cent less reflective when illuminated by M-type star, with respect to the solar case. Thus, we adopt a_c=0.40.

4 RESULTS

The models described in the previous section were applied to explore how the climate and habitability of Gl 514 b are affected by different sets of planetary and orbital configurations. For each set of climate simulations we calculate the surface temperature distribution, $T(\varphi, t)$, and the habitability index, h, for the three atmospheres described in subsection 3.4.

For each atmospheric composition we vary the surface pressure, $p_{\rm tot}$, to assess how the climate is affected by changes of the atmospheric column, $\mathcal{N}_{\rm atm} = p_{tot}/g$. This quantity represents the atmospheric mass per unit surface area and has a strong impact on the climate for two reasons. First, for a given atmospheric composition and in the investigated $p_{\rm tot}$ interval, the greenhouse effect increases with $\mathcal{N}_{\rm atm}$; in our model this effect is taken into account by the EOS RT calculations. Secondly, the efficiency of the atmospheric transport along the planet surface increases with $\mathcal{N}_{\rm atm}$; in our model this effect is accounted for by the diffusion term $\mathcal{D}$, which increases linearly with $\mathcal{N}_{\rm atm}$. It is worth noticing that, as long as Gl 514 b is a rocky super-Earth, the percent uncertainty in g is small, and does not affect significantly the estimates of $\mathcal{N}_{\rm atm} = p_{tot}/g$.

Since the atmospheres that we consider are CO_2-dominated, we also take into account the possibility that condensation of atmospheric CO_2 may occur. To this end we adopt the function for the saturation vapour pressure of CO_2 reported in Kasting (1991). The condensation of atmospheric CO_2 would drive a collapse of the atmosphere and the formation of CO_2 ices on the surface. The dashed areas in the figures shown in this section indicate regions of the parameter space where this effect is predicted to take place. If the atmosphere undergoes collapse, the surface habitability is compromised.

4.1 Dependence on planetary parameters

4.1.1 Surface distribution of oceans and continents

EOS-ESTM incorporates planet geography in a schematic way, assigning to each latitude zone a fractional coverage of oceans, f_o, which implies a fractional coverage of lands, $f_l = 1 - f_o$. To explore the effects of geography on habitability we first changed the global coverage of oceans, keeping f_o constant at all latitudes, and then we fixed the global coverage of oceans, changing f_o according to the latitude.

The results of the first test are shown in Fig. 3, where we show the variation of h as a function of f_o and $p_{\rm tot}$. The general trend is that as the coverage of oceans increases: (i) the range of habitable conditions broadens, embracing lower and lower atmospheric pressures; (ii) the habitability tends to rise with increasing CH_4 content. These trends can be explained as a result of the increasing thermal inertia of the climate system with increasing f_o. As the pressure increases, the efficient atmospheric diffusion combines with the high thermal inertia of the oceans, yielding year-long habitable conditions despite the relatively low instellation of Gl 514 b. For the model with higher CH_4 content these effects can be seen in the maps of seasonal-latitudinal evolution of surface temperature plotted at selected values of ocean cover and surface pressure (Fig. 4). Only at the highest pressure the collapse of the CO_2-dominated atmospheres can be prevented in all latitude zones.

For the second test, following Vladilo et al. (2013, 2015), we fixed the global ocean coverage, $f_o = 0.7$, and we considered two model geographies (1) an equatorial continent, and (2) a polar continent.In practice, the case (1) represents a continent located at latitudes within $\pm 25°$, whereas the case (2) represents a polar continent at latitudes below $-25°$. In Fig. 5 we show how these different types of model geographies introduce modest effects on the mean global annual temperature. Similarly, the mean annual habitability is almost the identical in the two continental configurations at all pressures. However, in the case of the polar continent, the fraction of habitable surface shows little seasonal oscillations, due to the formation of a larger ice cap in the presence of a polar continent. This behaviour

[5]To conduct this computation, we again employ the spectrum of AD Leo (M3V), for the sake of homogeneity with our choices regarding the surface albedos.

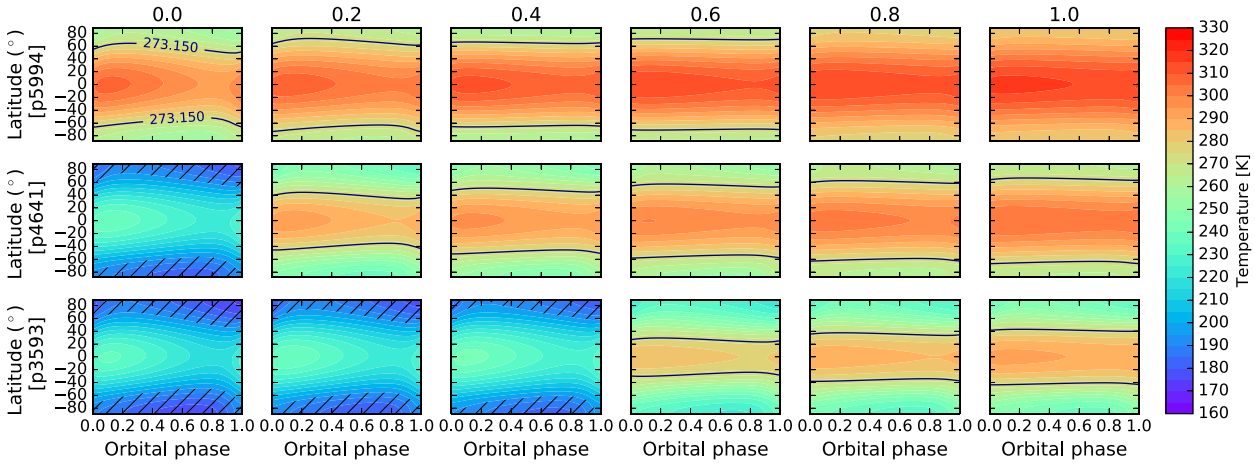

Figure 4. Seasonal and latitudinal maps of surface temperature obtained by extracting the results of Fig. 3c (case with 1 per cent CH_4) at constant values of ocean cover (from left to right: $f_o = 0$, 0.2, 0.4, 0.6, 0.8, and 1.0) and total pressure (from top to bottom: $p_{\rm tot}$ =5994, 4641, and 3593 mbar). For $p_{\rm tot} = 5994$ mbar, the equatorial habitable belt extends towards the poles with increasing f_o. For $p_{\rm tot} = 3593$ mbar, $T \geq$273.15 K only in a limited equatorial zone, for $f_o \geq 0.6$.

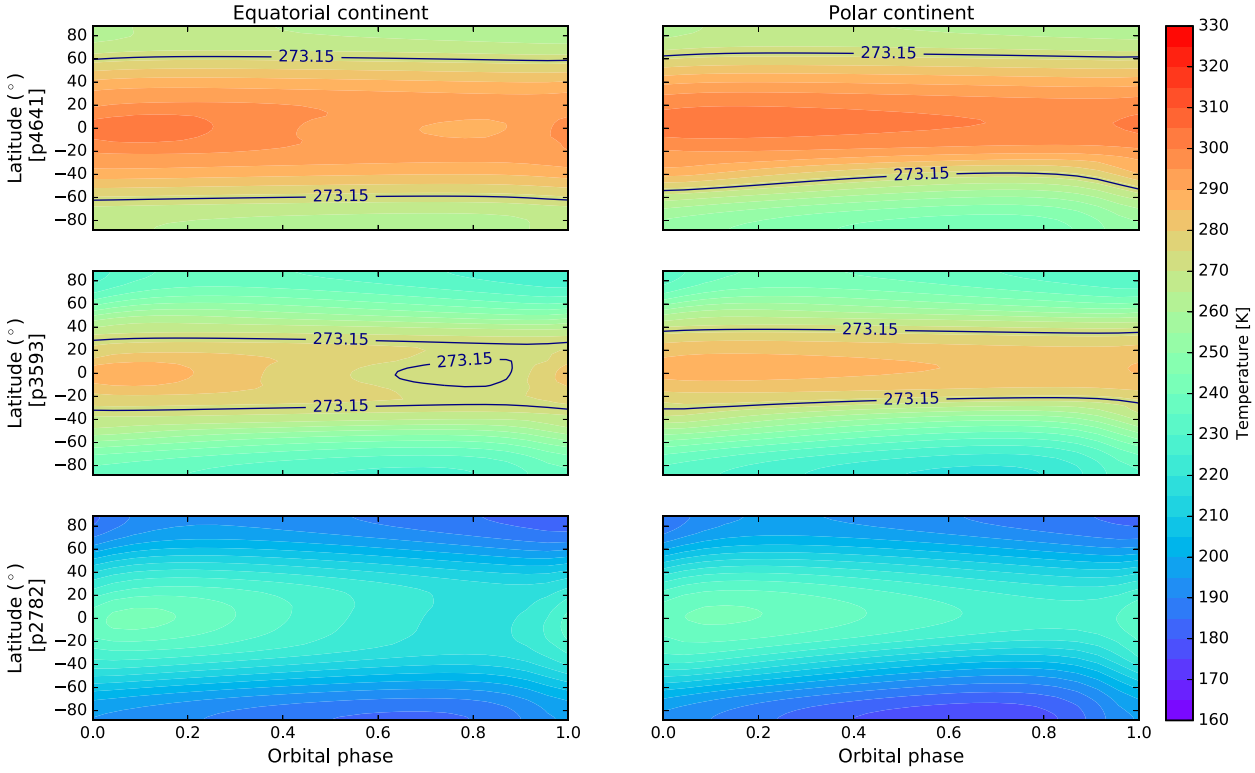

Figure 5. Seasonal and latitudinal evolution of the surface temperature of Gl 514 b for two model geographies at fixed ocean coverage (70 per cent) and three values of surface pressure in a CO_2-dominated atmosphere with 1 per cent of CH_4. Left panel: equatorial continent spread over all longitudes. Right panel: polar continent centred at latitude -90°. The surface pressure is 4.641 (top panel), 3.593 (central panel), and 2.782 (bottom panel) bar. For the remaining parameters we adopt $\epsilon = 23.44^\circ$, $P_{\rm rot} = 1$ d, and $\omega_{\rm peri} = 0^\circ$.

is probably due to the combination of two factors (i) the land has a lower thermal capacity (C_l=1 $\times$ 10^6 J m^{-2} K^{-1}) than the water (C_o=210 $\times$ 10^6 J m^{-2} K^{-1}) and (ii) the albedo of ice over ocean ($a_{\rm io}$ = 0.35) is much lower than that of ice over land ($a_{\rm il}$ = 0.52).

We conclude that the the global fraction of oceans coverage affects the climate more significantly than the latitudinal distribution of oceans and continents.

Aside for the mean annual values, we are also interested in studying the seasonal T variability, which in our model is directly related to the seasonal habitability of the planet. Since f_o impacts the overall thermal inertia of the planet, it plays a crucial role in shaping this value. This can be observed in Fig. 5 by comparing the cases with f_o = 0.0 and f_o = 1.0 at $p_{\rm tot}$ ~6.0 bar. In the former, $\Delta T \equiv T_{\rm max} - T_{\rm min}$ ~13 K at the tropical latitudes, that is, $\pm$ 23°, while in the

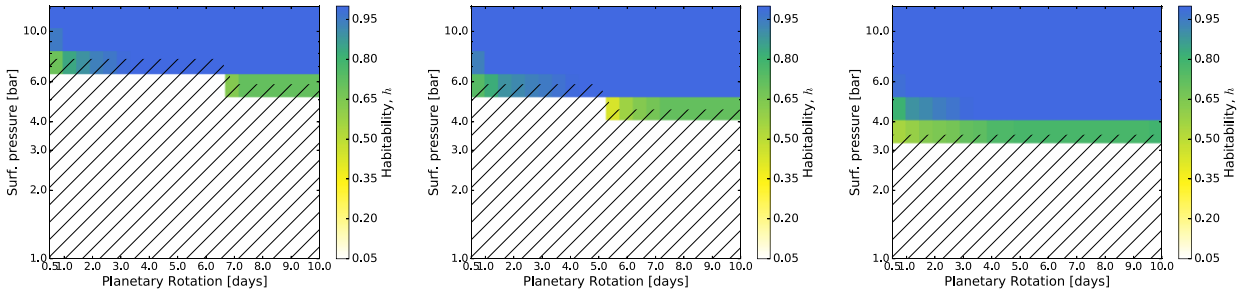

Figure 6. Predicted values of the habitability index, h, as a function of the planet rotation period and total surface pressure for three different atmospheric compositions. Left panel: CO_2-dominated; middle panel: CO_2+0.1 per cent CH_4; right panel: CO_2+1 per cent CH_4. For the remaining parameters we adopt $\epsilon = 23.44°$, $f_o = 0.75$, and $\omega_{\rm peri} = 0°$. The dashed areas indicate the parameter space in which atmospheric CO_2 condensates.

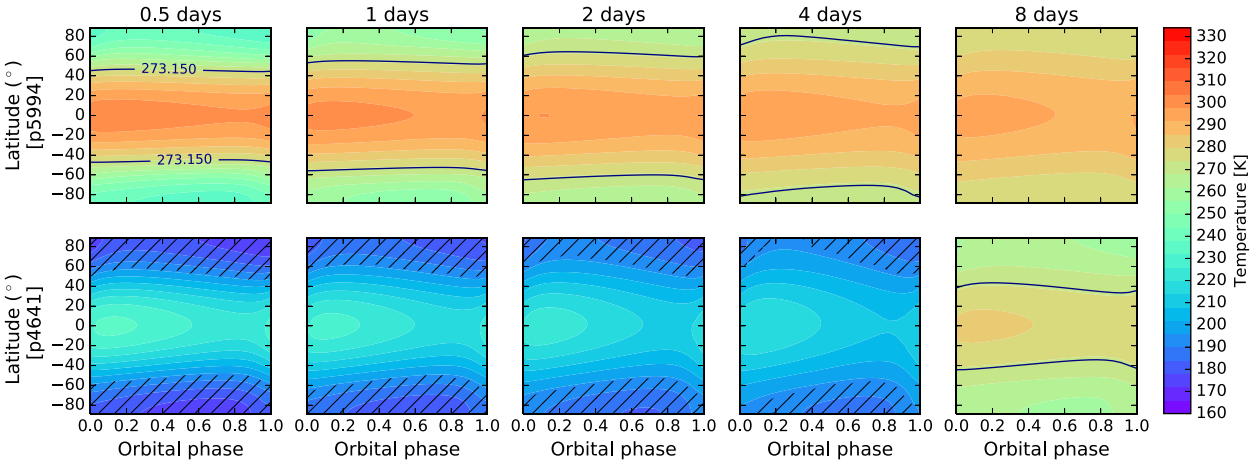

Figure 7. Seasonal and latitudinal maps of surface temperature obtained by extracting the results of Fig. 6b (case with 0.1 per cent CH_4) at constant values of planetary rotation period (from left to right: 0.5, 1, 2, 4, and 8 d) and total pressure (from top to bottom: $p_{\rm tot} = 5996$, and 4641 mbar).

latter it decreases to 3 K. If the ocean fraction is high it completely dominates the planetary heat capacity and, in fact, the effect of $p_{\rm tot}$ on ΔT becomes negligible. This is clear if we compare the cases with $p_{\rm tot}$ ∼6.0 bar and 3.6 bar, both of which show ΔT ∼3 K.

4.1.2 Rotation period

In a rotating planet, the Coriolis forces tend to damp the atmospheric energy transport from the equator to the poles, the effect becoming stronger with increasing angular velocity of rotation, $\Omega = 2\pi/P_{\rm rot}$. In EOS-ESTM this effect is incorporated in the diffusion term, which scales as $\mathcal{D} \propto \Omega^{-4/5}$ according to an analytic formulation of the latitudinal transport calibrated with 3D climate models (Vladilo et al. 2015). In Figs 6, 7, and 8 we show results of climate simulations of Gl 514 b performed by varying $P_{\rm rot}$ and total pressure, $p_{\rm tot}$. As a general trend, two effects are visible as the rotation period increases (i) the planet habitability tends to increase and (ii) the surface temperature is homogenized, particularly in the high-pressure regime (see top row of Fig. 8). This effect is expected because $\mathcal{D}$ also increases with $p_{\rm tot}$. On the extreme case of a rapid-rotating planet ($P_{\rm rot} = 0.5$ d) a habitable belt can built up at the equatorial zone for $p_{\rm tot} < 4.0$ bar (in the central left panel of the figure). At the other extreme of low rotation periods ($P_{\rm rot} = 8$ d) and $p_{\rm tot} > 4.0$ bar the habitability index is maximized (in the top-right panel of the figure). The simulations also show remarkable differences, depending on the adopted atmospheric composition. In the model with higher CH_4 content, the planet rotation period has a negligible impact on h, with a general trend of increasing h with decreasing $p_{\rm tot}$ (up to ∼3.5 bar). At low CH_4 content, we find an increase in the habitability with increasing $P_{\rm rot}$, with sudden transitions from $h \simeq 1$ to $h = 0$.

At variance with the global fraction of oceans, we find that the planetary rotation period has only a minor impact on the seasonal habitability. This effect is visible in Fig. 8 by comparing the two extreme cases tested here, $P_{\rm rot} = 0.5$ and 8 d, for the same $p_{\rm tot}$ ∼6.0 bar: at tropical latitudes, we find that in the former ΔT ∼4 K, while in the latter ΔT ∼3 K.

Tests with even a moderate variation, for example ∼30 per cent larger planetary radius (e.g. 2.1 $R_\oplus$), provide higher habitability indices even for ∼13 per cent lower surface pressure (e.g. ∼2.8 bar), in the case of a high methane content. This evidences the robustness of the model against variations of R_P. We obtain similar results also varying the other planetary and orbital parameters.

4.1.3 Axis obliquity

In the last two decades, several climatological studies (e.g. Williams & Pollard 2002; Dressing et al. 2010; Spiegel et al. 2010) have explored the role of obliquity on the planetary climate finding that larger values tend to increase the globally averaged temperature of a planet. In addition, Williams & Pollard (2003) found that planets with

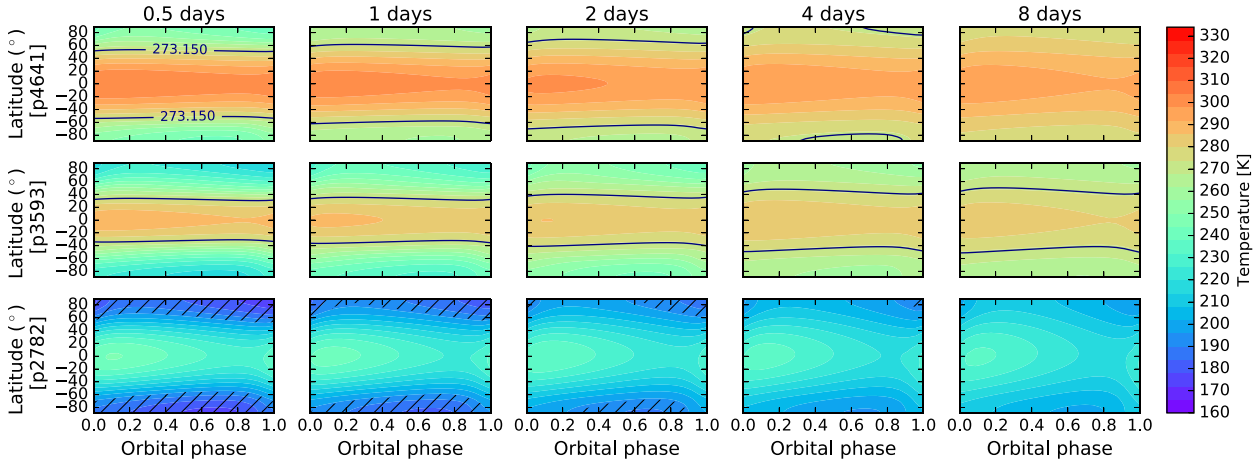

Figure 8. Seasonal and latitudinal maps of surface temperature obtained by extracting the results of Fig. 6c (case with 1 per cent CH_4) at constant values of planetary rotation period (from left to right: 0.5, 1, 2, 4, and 8 d) and total pressure (from top to bottom: $p_{\rm tot} = 4641$, 3593, and 2782 mbar).

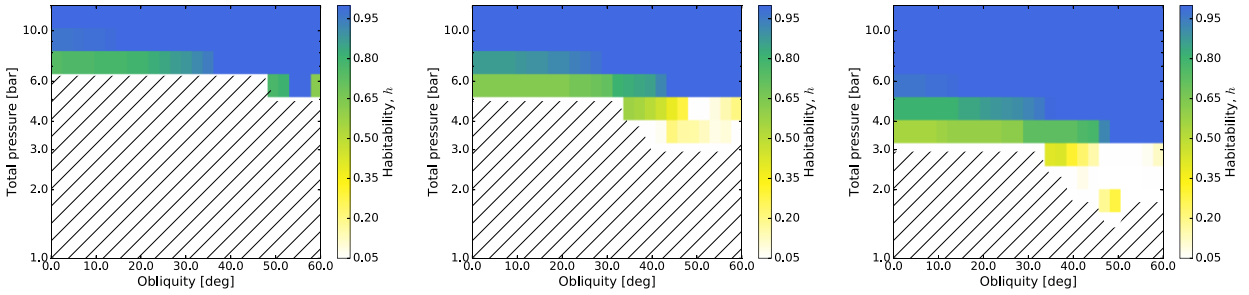

Figure 9. Predicted values of the habitability index, h, as a function of the axis obliquity and total surface pressure for three different atmospheric compositions. Left panel: CO_2-dominated; middle panel: CO_2+0.1 per cent CH_4; right panel: CO_2+1 per cent CH_4. For the remaining parameters we adopt $P_{\rm rot} = 1$ d, $f_o = 0.75$, and $\omega_{\rm peri} = 0°$. The dashed areas indicate the parameter space in which atmospheric CO_2 condensates.

high obliquity are less prone to experience extreme events, such as the runaway greenhouse instability or transition to a snowball state. In our study of Gl 514 b we varied ϵ from 0° to 60°. The resulting maps of habitability, h, versus obliquity and total atmospheric pressure is shown in Fig. 9 for the three atmospheric compositions considered in this work. The seasonal impact of these planetary configurations are shown in Figs 10 and 11.

Two general trends are seen in Fig. 9 (i) the habitability increases with increasing ϵ and (ii) the higher the concentration of methane in the atmosphere, the wider the range of habitability is. The former behaviour can be explained in the following way. The configuration at $\epsilon = 0°$ favours the formation of permanent ice caps in the polar regions, where the star is always at large Z. As the obliquity starts to increase, a larger fraction of polar regions undergo a period of higher instellation (lower Z) and this reduces the ice caps, increasing the habitability (see Figs 10 and 11). However, when the obliquity is as large as 60°, a permanent ice belt can build-up in the equatorial zones, leading to a decrease in the habitability (Fig. 10). Nonetheless, polar ice caps or equatorial ice belts tend to disappear as the pressure increases due to (i) the stronger greenhouse effect of thick atmospheres and (ii) the higher efficiency of the horizontal transport at high $p_{\rm tot}$, which tends to cancel gradients of surface temperature. Cases with very high obliquity ($\epsilon > 60°$) are not considered here since they would require a 3D treatment of the atmospheric energy transport.

As far as the seasonal variability is concerned, we find that planetary axis obliquity do not play a significant role. This was not expected since, as ϵ grows, both hemispheres are subject to larger and larger instellation variations during the orbit. In Fig. 11 we show that, for $\epsilon = 20°$ and $p_{\rm tot} \sim 3.5$ bar, $\Delta T \sim 3$ K at the tropical latitudes. At high axis obliquity ($\epsilon = 60°$), the seasonal variability is essentially identical ($\Delta T \sim 3$ K) but in this case is sufficient to bring T below 273.15 K for at least a part of the year, thus reducing the overall habitability. At $p_{\rm tot} \sim 2.8$ bar only the poles ($\phi \geq 82°$) are partially habitable ($\Delta T \sim 7$ K).

4.2 Dependence on orbital parameters

4.2.1 Eccentricity

The orbital eccentricity, e, impacts the mean annual flux, $\bar{S}$, received by a planet according to the law (e.g. Williams & Pollard 2002)

$$\bar{S} = \frac{L_\star}{4\pi a^2 (1-e^2)^{1/2}}, \tag{7}$$

where $L_\star$ is the luminosity of the host star and a the semimajor axis. Compared to a circular orbit, the mean instellation increases by a factor $(1-e^2)^{-1/2}$ and the maximum excursion of the instellation during the orbit grows as $[(1+e)/(1-e)]^2$, exceeding one order-of-magnitude when $e > 0.5$. Highly eccentric orbits generate seasons as the distance between the star and planet varies during the orbit.

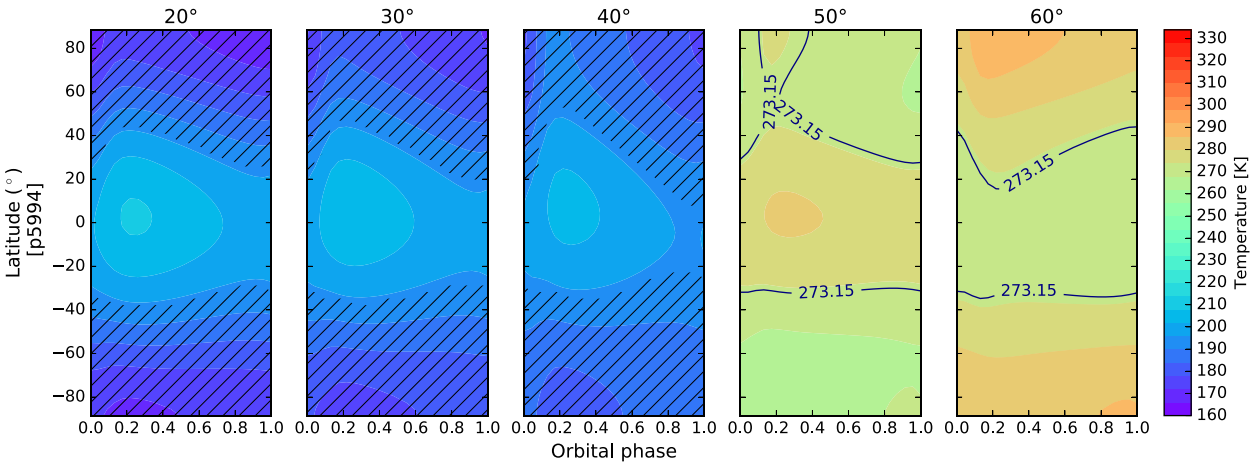

Figure 10. Seasonal and latitudinal maps of surface temperature obtained by extracting the results of Fig. 9a (case with 0 per cent CH_4) at constant values of axis obliquity (from left to right: $\epsilon = 20°$, 30°, 40°, 50°, and 60°) and total pressure $p_{\rm tot} = 5464$ mbar. Note that as the obliquity starts to increase, a larger fraction of polar regions undergo a period of higher instellation, increasing the global surface temperature. When $\epsilon = 50°$, an habitable belt can build up in the equatorial zones. Furthermore, habitable conditions are reached in the Northern hemisphere during the summer solstice. At higher obliquity, polar zones reduce the ice caps and increase habitability. However, at $\epsilon = 60°$ ice starts to form in the equatorial zones, decreasing h. The solid line indicate the limit within which water can be maintained in liquid form.

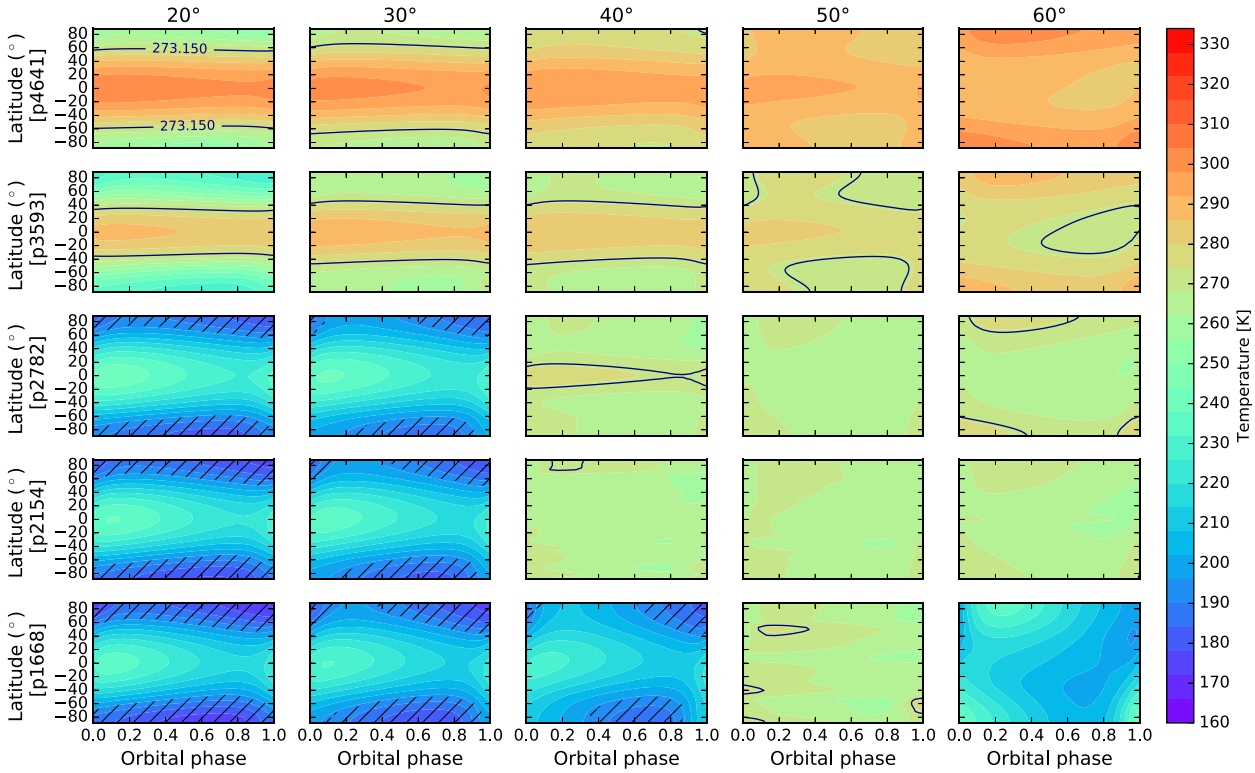

Figure 11. Seasonal and latitudinal maps of surface temperature obtained by extracting the results of Fig. 9c (case with 1 per cent CH_4) at constant values of axis obliquity (from left to right: $\epsilon = 20°$, 30°, 40°, 50°, and 60°) and total pressure (from top to bottom: $p_{\rm tot} = 5464$, 3593, 2782, 2154, and 1668 mbar). The solid line indicate the limit within which water can be maintained in liquid form.

Neglecting the obliquity effects discussed earlier, both planetary hemispheres will experience the same season as the instellation varies along the orbit: summer occurs at periastron, whereas winter at apoastron. The higher the eccentricity, the stronger the seasonal temperature excursions. Our climate simulations show how the orbital eccentricity may impact the habitability of Gl 514 b. In Fig. 12, we show the resulting map of the habitability index h in the plane (e, $p_{\rm tot}$). One can see that the range of atmospheric pressure favourable to habitability becomes wider as e increases. The central and right panels of Fig. 12 show that surface liquid water can persist at the highest eccentricities even for a moderate pressure ($p_{\rm tot} \sim$1000 mbar). For the sake of comparison, we report in Fig. 13 the resulting map

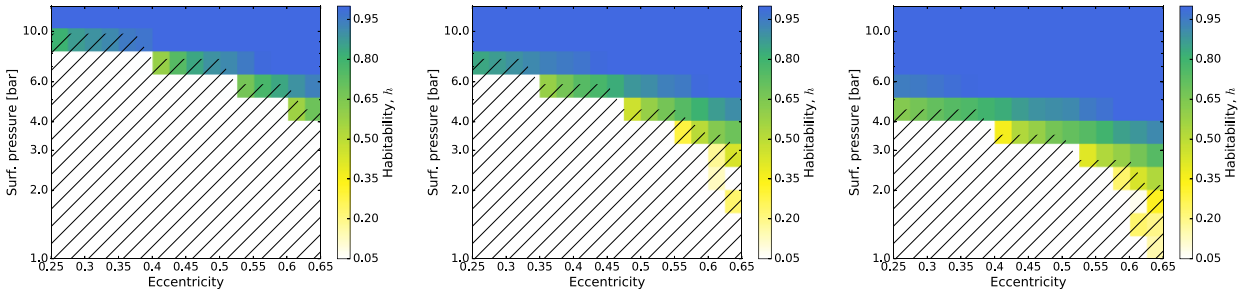

Figure 12. Predicted values of the habitability index, h, as a function of the eccentricity and total surface pressure for three different atmospheric compositions. Left panel: CO_2-dominated; middle panel: CO_2+0.1 per cent CH_4; right panel: CO_2+1 per cent CH_4. For the remaining parameters we adopt $P_{\rm rot} = 1$ d, $f_o = 0.75$, $\epsilon = 23.44^\circ$, and $\omega_{\rm peri} = 270^\circ$. The dashed areas indicate the parameter space in which atmospheric CO_2 condensates.

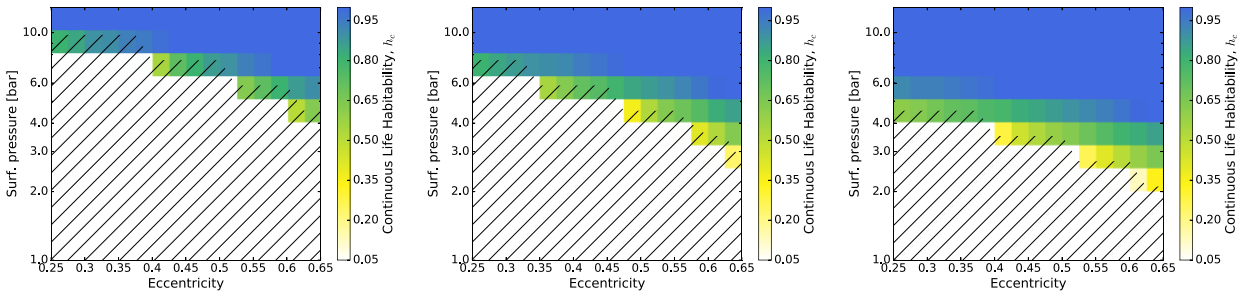

Figure 13. Similar to Fig. 12 but adopting the continuous habitability, h_c.

of h_c for the same plane (e, p_{tot}) of Fig. 12. One general trend is visible: $h_c = 0$ for higher p_{tot}, at very high e, due to the more restrictive definition of the index. As a conclusion, the habitability becomes restricted to a narrow range of surface pressures. The earlier results show that, within the current uncertainty in the measurement, $e = 0.45^{+0.15}_{-0.14}$ (Damasso et al. 2022), the seasonal impact of the eccentricity on habitability could be quite strong.

The eccentricity as well as the global ocean coverage significantly impacts the seasonal habitability. The larger the eccentricity, the more significant is the seasonal excursion of the surface temperature. For the model with higher CH_4 content and $p_{\rm tot}$ ~4.6 bar, ΔT increases by ~4 K between $e = 0.25$ and $e = 0.65$ at the tropical latitudes, bringing the total variation in the latter case to 6 K.

4.2.2 Argument of periastron

The argument of periastron, $\omega_{\rm peri}$, is one of the six orbital elements univocally describing an orbit. In the most widely used definition, it represents the angle between the ascending node and the periastron, measured in the direction of motion. The value of $\omega_{\rm peri}$ impacts the habitability by modulating the intensity of the seasonal temperature variations at surface, especially when both the eccentricity and obliquity are high. For cylindrically symmetric planets, such as those simulated by seasonal-latitudinal EBMs, there are three possible distinct scenarios (i) if $\omega_{\rm peri} = 0^\circ$ or 180°, then the planet will be at its closest approach to the central body when it crosses the equatorial plane from South to North, that is, at the equinox; (ii) if $\omega_{\rm peri} = 90^\circ$, the periastron will occur at the Southern hemisphere summer solstice; (iii) if $\omega_{\rm peri} = 270^\circ$ the periastron will occur at the Northern hemisphere summer solstice. If the two hemispheres are identical in terms of surface features (e.g. the ocean coverage), then the overall climatology of cases (ii) and (iii) will be essentially the same. In particular, in (ii) and (iii), seasonal temperature variations in one of the two hemispheres will be stronger than in the other, since the effect of eccentricity and obliquity are compounded. Alternatively, in case (i) both hemispheres will experience the same seasonality. A change in the magnitude of seasonal temperature variations can, for example, facilitate the condensation of the CO_2 atmosphere at the surface, as demonstrated for the early Mars scenario (Simonetti et al. 2024). Given that it is not possible to determine the direction of any exoplanetary spin axis yet, $\omega_{\rm peri}$ must be treated as a completely free parameter. For transiting exoplanets, an 'argument of periastron' is generally available, but it represents the angle between the position of the periastron and the line of sight. It is, therefore, a completely different quantity.

Here, we investigate two of the three extreme configurations listed above, namely $\omega_{\rm peri} = 0^\circ$ and $\omega_{\rm peri} = 270^\circ$:

(i) for $\omega_{\rm peri} = 0^\circ$, the Northern hemisphere (NH) autumnal equinox and the Southern hemisphere (SH) spring equinox will occur at the periastron, with the opposite occurring at apoastron. By construction, the seasonal effects of eccentricity and obliquity will be out of phase by 90° from one another: the global summer/winter generated by eccentricity does not coincide with the hemispheric summer/winter generated by obliquity;

(ii) for $\omega_{\rm peri} = 270^\circ$, the NH winter solstice and the SH summer solstice will occur at the periastron, with the opposite occurring at apoastron. In this case, the global summer/winter generated by eccentricity coincides with the Southern hemispheric summer/winter generated by obliquity. As a result, seasonality will be damped for the NH and amplified for the SH.

Results from simulations performed with these two values of $\omega_{\rm peri}$ are shown in Figs 9 ($\omega_{\rm peri} = 0^\circ$) and 14 ($\omega_{\rm peri} = 270^\circ$). The resulting maps of habitability are remarkably similar in spite of the

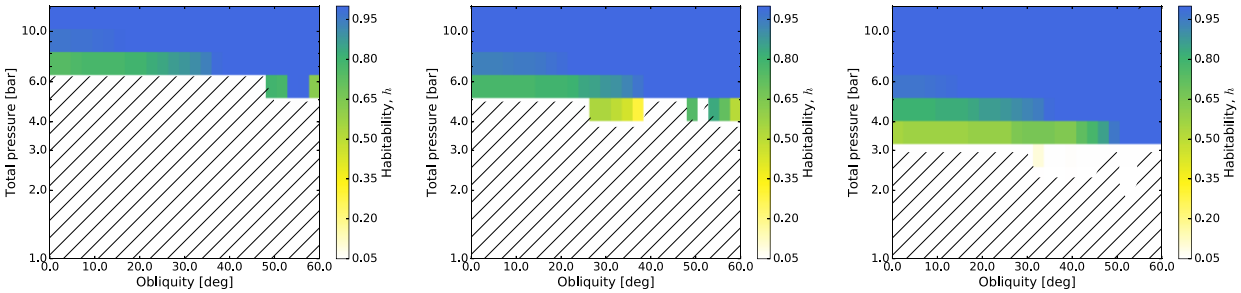

Figure 14. Predicted values of the habitability index, h, as a function of the axis obliquity and total surface pressure for three different atmospheric compositions. Left panel: CO_2-dominated; middle panel: CO_2+0.1 per cent CH_4; right panel: CO_2+1 per cent CH_4. For the remaining parameters we adopt $P_{\rm rot} = 1$ d and $f_o = 0.75$, and $\omega_{\rm peri} = 270^\circ$. The dashed areas indicate the parameter space in which atmospheric CO_2 condensates.

significantly different orbital configuration. This result is probably due to the high fraction of oceans adopted in these simulations ($f_o = 0.75$), since the high-thermal capacity of water tends to damp seasonal variations,decreasing them by around 2 K at the tropical latitudes in the $\epsilon = 23.4^\circ$ case (see Figs 10 and 15). In the latter configuration, when $\epsilon \geq 50^\circ$, the surface temperature reaches habitable conditions during the SH summer solstice. During this period the planet lies in proximity of the periastron, thus, as ϵ increases, the southern pole temperature rises. In this configuration one can see that (i) in the NH, T is quite-constant ($\sim$273 K) along the orbit because the NH summer is relatively long, (ii) in the SH, $T \geq$ 273 K only for $\sim$ 20 per cent of the orbit, namely during the winter solstice.

The impact of the argument of periastron on seasonal habitability can be non-negligible if the planet is predominantly covered by lands. An example can be seen in Fig. 16, where we show a case with small ocean coverages ($f_o = 0.2$). One can see that, depending on the orbital configuration, the northern/southern poles of planet may be habitable or not. Note that the higher the axis obliquity the more this effect is emphasized.

5 DISCUSSION

5.1 Stellar activity and habitability

In the assessment of the habitability of Gl 514 b, the strong activity of M-type stars can play a crucial role. A planet in the close-in HZ of an M-type star will be continuously bombarded with XUV radiation. As a result, the planet may loose oceans, ending up dessicated and void of surface life (Luger et al. 2015; Shields, Ballard & Johnson 2016). Strong XUV irradiation can also enhance exospheric temperatures, making thermal escape a dominant mechanism of atmospheric loss for planets around M dwarfs at early times (Lammer et al. 2007; Sanz-Forcada et al. 2010; Luger et al. 2015; Meadows & Barnes 2018). According to Modi, Estrela & Valio (2023), photoevapouration of the planetary atmosphere is the dominant mechanism capable of partially stripping the primordial H/He envelope, for planets orbiting early-type M dwarfs at the outer edge of the HZ. The effective habitability of Gl 514 b may therefore depend on the initial volatile inventory and the degassing of volatiles from the planet's interior, which could help replenish the atmosphere and sustain surface water, potentially compensating for the early-atmospheric loss. Over the last decades, the occurrence of 2–4 $R_\oplus$ planets in the Kepler field (e.g. Howard et al. 2012) has underscored the ubiquity of inward disc-driven migration in planetary systems, suggesting that these systems likely did not form *in situ* (Cossou et al. 2014). In this way, Luger et al. (2015) suggested that is possible for atmospheric escape processes to remove the thick H/He envelopes of mini-Neptunes, that reside in the HZ, effectively turning them into volatile-rich Earths and super-Earths, referring them as "habitable evapourated cores". Finally, we note that the eccentricity of Gl 514 b may be the result of a late-scattering event. In this case, changes in the planet's orbital parameters would have heavily affected the planet's climate equilibrium (Kaib & Raymond 2024).

During the early-active phase the stellar magnetic field is strong enough to reduce the size of planetary magnetosphere, exposing more of the planet's atmosphere to erosion (Vidotto et al. 2013; Garraffo, Drake & Cohen 2016; Airapetian et al. 2017). Atmospheric erosion can be greatly enhanced by stellar flares and associated coronal mass ejections (CMEs) resulting from stellar activity. From a biological point-of-view, the impact of a large amount of XUV radiation hitting the planet can be both harmful and indispensable to life. On one side, it can destruct biomolecules (Sagan 1973), and damage various species of proteins and lipids (Cockell 1998; Buccino, Lemarchand & Mauas 2007). On the other side, UV radiation might have played a key role in the origin of life, as a crucial ingredient for pre-biotic photochemistry (Ehrenfreund et al. 2002; Buccino et al. 2007; Powner, Gerland & Sutherland 2009; Rimmer et al. 2018; Spinelli et al. 2023).

In the course of evolution, stellar winds remove angular momentum, spinning the stars down (Vidotto et al. 2013). This mechanism acts in the way that early-M dwarfs, such as Gl 514, are active/rapidly rotating for a much shorter time ($\sim$1 Gyr) than the mid- ($\sim$4–6 Gyr), and late-M dwarfs (>7 Gyr) (West et al. 2008; Irwin et al. 2011; Gunning et al. 2014; Shields et al. 2016). Based on the rotation period and the level of activity, we estimate that the approximate age of Gl 514 is $\sim$3.0 $\pm$ 0.9 and $\sim$3.5 $\pm$ 1.2 Gyr, respectively (Section 2.1.1). This suggests that the star may be relatively inactive (e.g. West et al. 2008), with fewer star-spots, less-energetic flares (Hawley et al. 2014), and lower XUV flux. In this respect, the possibility that the habitability of Gl 514 b is not compromised by stellar activity is much higher than in the case of the relatively numerous planets found in the HZ around late-M dwarfs, since these stars preserve a high-level of activity for a much longer time and their HZs lie even closer to the star.

5.2 Planetary properties and habitability

In addition to the climate system, the habitability is influenced by other planetary properties, and in particular by the magnetic field (Haghighipour 2011; Vidotto et al. 2013; Driscoll & Barnes 2015; Meadows & Barnes 2018). A strong magnetic field offers protection

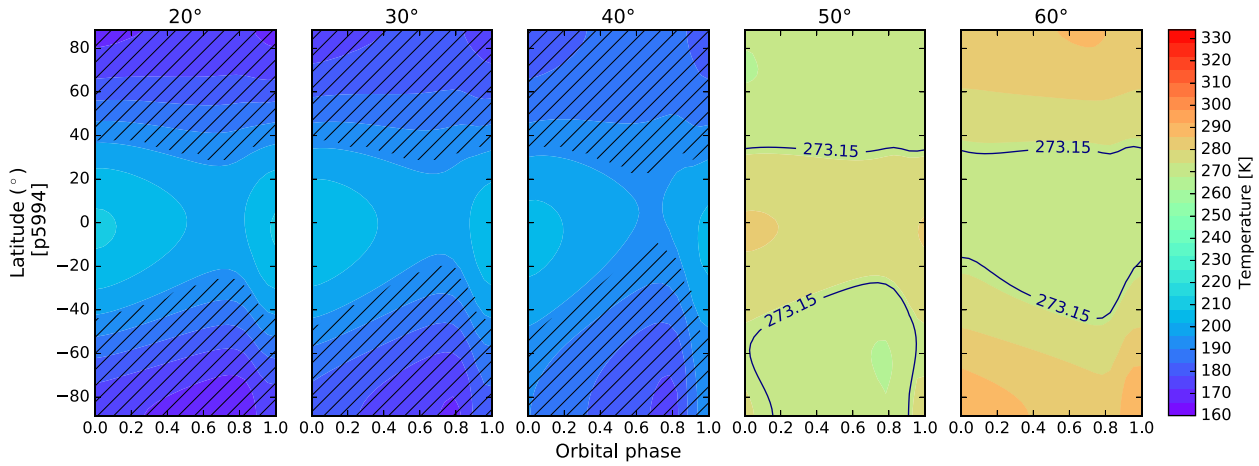

Figure 15. Seasonal and latitudinal maps of surface temperature obtained by extracting the results of Fig. 14a (case with 0 per cent CH_4) at constant values of axis obliquity (from left to right: 20°, 30°, 40°, 50°, and 60°) and total pressure $p_{\rm tot} = 5994$ mbar. Note that as the obliquity starts to increase, a larger fraction of polar regions undergo a period of higher instellation, increasing the global surface temperature. When $\epsilon = 50°$, an habitable belt can build up in the equatorial zones. Furthermore, habitable conditions are reached in the Northern hemisphere during the summer solstice. At higher obliquity, polar zones reduce the ice caps and increase habitability. However, at $\epsilon = 60°$ ice starts to form in the equatorial zones, decreasing the habitability.

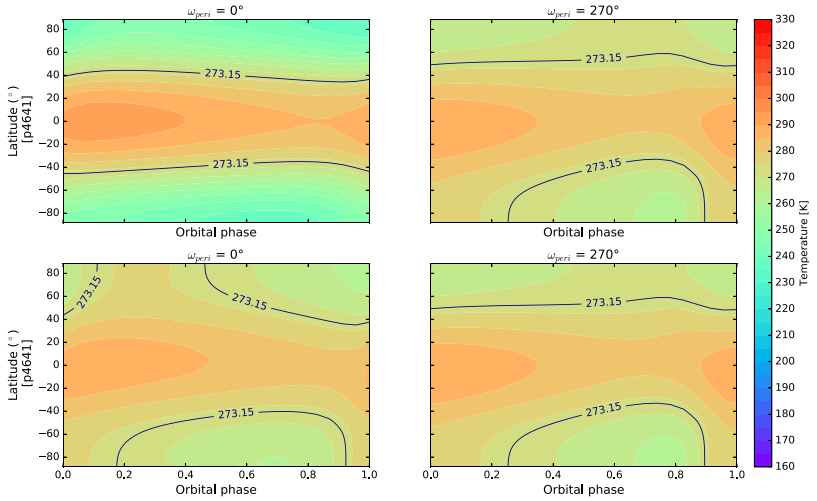

Figure 16. Seasonal and latitudinal maps of surface temperature for the case with $f_o = 0.2$, $P_{\rm rot} = 1$ d, and 1 per cent CH_4 at constant values of argument of periastron (from left to right: 0° and 270°), axis obliquity (from top to bottom: 23.4° and 45°) and total pressure $p_{\rm tot} = 4641$ mbar.

from stellar wind erosion of the planet atmosphere (Driscoll & Bercovici 2013) and from CMEs (Kay, Opher & Kornbleuth 2016). The magnetic field is also essential for the long-term persistence of surface life, protecting the orbiting planet from harmful high-energy radiation and cosmic rays penetrating the planetary surface (Grießmeier et al. 2005; Dartnell et al. 2011; Grießmeier et al. 2015).

Whether or not a significant magnetic field is present in super-Earths, such as Gl 514 b, is an active topic of research (e.g. Gaidos et al. 2010; Tachinami, Senshu & Ida 2011; Stamenković et al. 2012). Generally, planetary magnetic fields arise from a dynamo mechanism which requires rotation, a core of liquid iron and a vigorous convection process (Stevenson 2010; Haghighipour 2011). The higher the planetary mass, the lower the efficiency of the full mantle convection, so that heat in deep interiors of super-Earths is transferred by conduction rather than convection (Stamenković et al. 2012; Airapetian et al. 2017), reducing the magnetic dynamo. The strength of a magnetic field in super-Earths crucially depends on as yet unverified assumptions, such as the initial thermal profile and the viscosity law (Stamenković et al. 2012). Also planetary rotation affects the evolution of the dynamo, and slowly rotating super-Earths may exhibit weak magnetic fields, even though their dipoles may endure for more extended periods (Zuluaga & Cuartas 2012). Other studies suggest that the planetary rotation period may determine whether the generated magnetic field is dipolar or multipolar, the fraction of dipolar field possibly depending on the local Rossby number (Vidotto et al. 2013).

Since we do not know the internal structure and rotation period of Gl 514 b, it is hard to understand to which extent a protective magnetic field could be present. However, the atmospheres of super-Earths are likely to be relatively thick, reducing the risk of atmospheric escape. At the same time, a thick atmosphere shields the planetary surface from high-energy cosmic particles, the effect becoming stronger with increasing atmospheric columnar mass (Grießmeier et al. 2005). All the planetary properties that in our

simulations yield habitable conditions for Gl 514 b are characterized by an atmospheric columnar mass, $p_{\rm tot}/g$, in excess of the Earth's value. This guarantees an effective shield from cosmic rays even for a modest value of the planetary magnetic dipole (Atri, Hariharan & Grießmeier 2013).

5.3 Extreme seasonal variations and habitability

The simulations presented in subsection 4.2.1 show that at the higher end of the eccentricity interval, the habitability of Gl 514 b tend to increase despite the somewhat stronger seasonal excursions in T. A more detailed analysis of the results shows that this is possible because these seasonal excursions are not actually very large in the first place. In fact, for most combinations of parameters, ΔT at low latitudes is $\lesssim 6$ K, which is consistent with the value derived from the ERA5 Earth observations (Hersbach et al. 2020). The quantity that causes the largest change in the strength of seasonality is f_o which, when reduced to 0, drives ΔT to 13 K. This is somewhat expected due to the interplay between the relatively high thermal capacity of even a shallow slab of water and the relatively short orbital period of the planet. However, the generally modest, Earth-like temperature swings come as a surprise and supports the idea that even eccentric super-Earths can be potential targets for the search of biosignatures.

It is also worth noticing that even the presence of intense thermal cycles (including water phase changes) does not seem to preclude the existence of life, even though their impact would not be negligible (McKay 2014). In fact, the set of space experiments called Lithopanspermia (Sancho et al. 2007) have demonstrated the resilience of lichens and bacteria, underlining their ability to endure harsh conditions in outer space thanks to their symbiotic nature and protection provided by the cortex (de la Torre et al. 2010). In a broader context, similar experiments have shown that several terrestrial organisms can survive to prolonged exposure to extreme temperature conditions, alongside vacuum, UVC irradiation, and cosmic rays (Kane & Gelino 2012).

A periodic increase of the sea surface temperature resulting from highly eccentric orbits may even foster a 'superhabitable' environment with sustained marine biological productivity, since the transfer of particulate organic carbon from the surface to deep ocean layers would be more efficient, influencing the nutrient concentrations in the deeper and surface layers (Jernigan et al. 2023). In this scenario, the more nutrients are recycled, the greater the production/persistence of biosignatures (e.g. O_2 and CH_4), which are particularly favourable for exoplanet life detection (Lovelock 1965). When local favourable conditions exist, the transport of these gases from the marine environment to the atmosphere may lead to seasonal variations in atmospheric composition, providing an opportunity to directly quantify biological fluxes (e.g. Olson et al. 2018). Owing to the sensitivity of ocean dynamics to planetary parameters, the rotation period, axis obliquity, and atmospheric pressure too play a role in regulating the nutrient supply for the surface biosphere. As an example, the nutrients up-welling is predicted to be enhanced in planets that rotate slower and have higher $p_{\rm tot}$, ϵ or e than Earth (Olson, Jansen & Abbot 2020). However, high eccentricity exerts a more pronounced influence on marine biological productivity than high obliquity (Olson et al. 2020).

In summary, the same conditions that, according to our results (Section 4), increase the habitability of Gl 514 b – high eccentricity, high ocean cover, high atmospheric pressure, high obliquity – can also provide an environment able to enrich the atmosphere with biological signatures that, in principle, could be detectable with spectroscopic observations.

6 CONCLUSIONS AND FUTURE PROSPECTS

Gl 514 b is as an excellent benchmark for understanding the potential climate states and habitability of nearby super-Earths in eccentric orbits. In the present work, we have applied our climate model, EOS-ESTM, to investigate which range of planetary properties would allow this planet to have habitable conditions. To this end, we employed a habitability index dependent on the surface temperature, which was computed by complementing the measured observational quantities with a parametrization of currently unknown planetary (e.g. geography, rotation period, axis obliquity), orbital (e.g. eccentricity, argument of periastron), and atmospheric (e.g. surface pressure, chemical composition) quantities. By assuming that the planet has an internal composition similar to that of the Earth, we performed our multiparametric exploration by adopting values of radius, $R_P = 1.6\,{\rm R}_\oplus$, and gravity, $g = 2.1\,{\rm g}_\oplus$. As far as the albedo properties are concerned, we estimated theoretical reflectances of several type of atmospheres and planetary surfaces illuminated by an early-type M-dwarf, such as the central star Gl 514. We tested three sets of CO_2-dominated atmospheres, each one with its own CH_4 concentration ($x_{\rm CH4}$: 0 per cent, 0.1 per cent, and 1 per cent), varying the total surface pressure in the range $p_{\rm tot} \in (1, 13)$ bar.

The main results can be summarized as follows

(i) in the range of orbital eccentricity consistent with the observations ($e = 0.45^{+0.15}_{-0.14}$), the impact of the eccentricity on habitability is important. The higher e, the wider the range of atmospheric pressure favourable to habitability becomes, down to a moderate pressure ($p_{\rm tot} \sim 1$ bar). We find that the impact on habitability of Gl 514 b of eccentricity variations is higher than that induced by variations of other key planetary quantities, such as obliquity.

(ii) When the obliquity is increased the planet experiences stronger seasonal excursions of surface temperature, that is, a larger fraction of polar regions undergo periods of high daily-averaged instellation, reducing the ice caps and increasing the habitability. For the model with higher CH_4 content, habitable conditions are reached for $p_{\rm tot} \sim 1.6$ bar and $\epsilon = 50^\circ$.

(iii) The habitability index decreases when ϵ reaches 60° because a permanent ice belt builds up in the equatorial zones.

(iv) The impact of higher obliquity tends to disappear as the surface pressure increases due to the high-efficiency of the horizontal energy transport, that removes temperature gradients on the planet surface.

(v) The high thermal capacity of oceans tends to damp seasonal variations at low latitudes down to modern Earth-like values (∼6 K). This is true even for modest cover fractions ($f_o \geq 0.4$). As such, oceans tend to substantially mute the relatively minor effect of $\omega_{\rm peri}$ variations, which are negligible in our calculations.

(vi) A long planetary rotation period increases the meridional energy transport, damping gradients of surface temperature, particularly in the high-pressure regime. In the model with higher CH_4 content, $P_{\rm rot}$ has a negligible impact on h, with a general trend of increasing h with decreasing $p_{\rm tot}$ (up to ∼3.5 bar). At low CH_4 content, h increases with increasing $p_{\rm tot}$, with sudden transitions from $h \simeq 1$ to $h = 0$.

(vii) The higher the global coverage of oceans, the more habitable the planet is. This is clearly due to the fact that oceans are darker than bare soil and the planet is, on average, cold.
For the model with higher CH_4 content, the habitability index is nearly 1 up to $p_{\rm tot} \sim 3.5$ bar, for $f_o = 1$. At low CH_4 content, the same result is obtained for $p_{\rm tot} \sim 6.0$ bar.

(viii) The latitudinal specific distribution of continents has a modest impact on the mean global annual temperature and generates

negligible seasonal temperature oscillations. Its impact on the climate of Gl 514 b is less significant with respect to the global coverage of oceans.

As a general trend, we underline that remarkable differences exist between the low- and high-concentration of CH_4 as well as between the low- and high-pressure regimes. This result is expected since both the higher greenhouse effect of thick atmospheres composed of CO_2 and CH_4 and the higher efficiency of the horizontal transport at high p_{tot} are well-known. Damped temperature gradients both in latitude and in time favour habitability, at least in this specific case.

Future observations may help to constrain the actual range of stellar, orbital, and planetary properties that affect the habitability of Gl 514 b. Asteroseismology obtained by extensive monitoring of nearby bright stars with PLATO (Rauer et al. 2014) may help to measure the age of Gl 514 and cast light on the evolutionary status of Gl 514 b. The large uncertainty on the eccentricity can be reduced by a long term sequence of radial-velocity measurements. So far, we cannot completely exclude that the planet is transiting (Damasso & Nardiello 2022), in which case we would be able to constrain radius, mass, and internal structure. Searches for transits might be performed with PLATO, during the 'Step and stare' Observation Phase. Transits could also be used to search for the Rossiter–McLaughlin (RM) effect (McLaughlin 1924; Rossiter 1924) which, in principle, may constrain the sky-project spin-orbit angle, the rotational spin direction of exoplanets, and the presence of an exomoon (Simon et al. 2010; Zhuang, Gao & Yu 2012), which can stabilize the planet's axis tilt. According to Nikolov & Sainsbury-Martinez (2015), during the secondary eclipses a strong and detectable RM signal can be measured to derive the planet rotation rate and axial tilt. Near-UV transit observations might also provide a useful tool in determining planetary magnetic field intensities (Ben-Jaffel et al. 2022). Moreover, high-contrast imaging of Gl 514 b is expected to become feasible with the Extremely Large Telescope (ELT) (see Damasso et al. 2022, for more details). The perspectives opened by these observational developments suggest that we will be able to assess the actual habitability of planets similar to Gl 514 b as long as they transit in front of their host star.

DATA AVAILABILITY

The data used for this article will be shared on reasonable request to the corresponding author.

REFERENCES

Abe Y., Abe-Ouchi A., Sleep N. H., Zahnle K. J., 2011, Astrobiology, 11, 443
Airapetian V. S., Glocer A., Khazanov G. V., Loyd R. O. P., France K., Sojka J., Danchi W. C., Liemohn M. W., 2017, ApJ, 836, L3
Astudillo-Defru N., Delfosse X., Bonfils X., Forveille T., Lovis C., Rameau J., 2017a, A&A, 600, 13
Astudillo-Defru N. et al., 2017b, A&A, 602, 88
Atri D., Hariharan B., Grießmeier J.-M., 2013, Astrobiology, 13, 910
Bailer-Jones C. A. L., Rybizki J., Fouesneau M., Mantelet G., Andrae R., 2018, AJ, 156, 58
Baraffe I., Chabrier G., Allard F., Hauschildt P. H., 1998, A&A, 337, 403
Baranov Y. I., Vigasin A. A., 1999, Journal of Molecular Spectroscopy, 193, 319
Barnes R., 2017, Celestial Mechanics and Dynamical Astronomy, 129, 509
Barry D. C., Cromwell R. H., Hege E. K., 1987, ApJ, 315, L264
Ben-Jaffel L. et al., 2022, Nature Astron., 6, 141
Biasiotti L. et al., 2022, MNRAS, 514, 5105
Brun P., Zimmermann N. E., Hari C., Pellissier L., Nikolaus Karger D., 2022, Earth System Science Data, 14, 5573
Buccino A. P., Lemarchand G. A., Mauas P. J. D., 2007, Icarus, 192, 582
Catling D. C., Kasting J. F., 2017, Atmospheric Evolution on Inhabited and Lifeless Worlds. Cambridge Univ. Press, Cambridge
Chassefière E., Langlais B., Quesnel Y., Leblanc F., 2013, Journal of Geophysical Research (Planets), 118, 1123
Clough S. A., Kneizys F. X., Davies R. W., 1989, Atmospheric Research, 23, 229
Cockell C. S., 1998, Journal of Theoretical Biology, 193, 717
Cossou C., Raymond S. N., Hersant F., Pierens A., 2014, A&A, 569, 56
Damasso M., Nardiello D., 2022, Research Notes of the American Astronomical Society, 6, 184
Damasso M. et al., 2022, A&A, 666, A187
Dartnell L. R., Storrie-Lombardi M. C., Mullineaux C. W., Ruban A. V., Wright G., Griffiths A. D., Muller J.-P., Ward J. M., 2011, Astrobiology, 11, 997
de la Torre R. et al., 2010, Icarus, 208, 735
Deitrick R., Haqq-Misra J., Kadoya S., Ramirez R., Simonetti P., Barnes R., Fauchez T. J., 2023, The Planetary Science Journal, 4, 39
Dickey J. O. et al., 1994, Science, 265, 482
Ding N. et al., 2021, Remote Sensing, 13, 1906
Dressing C. D., Spiegel D. S., Scharf C. A., Menou K., Raymond S. N., 2010, ApJ, 721, L1295
Driscoll P. E., Barnes R., 2015, Astrobiology, 15, 739
Driscoll P., Bercovici D., 2013, Icarus, 226, 1447
Efroimsky M., 2012, ApJ, 746, L150
Ehrenfreund P. et al., 2002, Rep. Prog. Phys., 65, 1427
Engle S. G., Guinan E. F., 2023, ApJ, 954, L50
Enomoto T., 2007, JAMSTEC Report of Research and Development, 6, 21
Etiope G., Ehlmann B. L., Schoell M., 2013, Icarus, 224, 276
Fetherolf T. et al., 2023, ApJS, 268, 4
Fischer D. A., Howard A. W., Laughlin G. P., Macintosh B., Mahadevan S., Sahlmann J., Yee J. C., 2014, in Beuther H., Klessen R. S., Dullemond C. P., Henning T., eds, Protostars and Planets VI. University of Arizona Press, Tucson, AZ, p. 715
Fortney J. J., Marley M. S., Barnes J. W., 2007, ApJ, 659, L1661
Fuhrmeister B. et al., 2019, A&A, 623, 24
Gaia Collaboration, 2021, A&A, 649, 1
Gaidos E., Conrad C. P., Manga M., Hernlund J., 2010, ApJ, 718, L596
Gaillard F., Scaillet B., 2014, Earth Planet. Sci. Lett., 403, 307
Garraffo C., Drake J. J., Cohen O., 2016, ApJ, 833, L4
Giggenbach W. F., 1996, Chemical Composition of Volcanic Gases. Springer, Berlin, Heidelberg, Germany
González-Álvarez E. et al., 2023, A&A, 675, 177
Gordon I. E. et al., 2022, J. Quant. Spec. Radiat. Transf., 277, 107949
Grießmeier J. M., Stadelmann A., Motschmann U., Belisheva N. K., Lammer H., Biernat H. K., 2005, Astrobiology, 5, 587
Grießmeier J. M., Tabataba-Vakili F., Stadelmann A., Grenfell J. L., Atri D., 2015, A&A, 581, 44
Grimm S. L. et al., 2021, ApJS, 253, 30
Gruszka M., Borysow A., 1997, Icarus, 129, 172
Gruszka M., Borysow A., 1998, Molecular Physics, 93, 1007
Gunning H. C., Schmidt S. J., Davenport J. R. A., Dhital S., Hawley S. L., West A. A., 2014, PASP, 126, 1081
Haghighipour N., 2011, Contemporary Physics, 52, 403
Hawley S. L., Gizis J. E., Reid I. N., 1996, AJ, 112, 2799
Hawley S. L., Davenport J. R. A., Kowalski A. F., Wisniewski J. P., Hebb L., Deitrick R., Hilton E. J., 2014, ApJ, 797, L121
Hersbach H. et al., 2020, Quarterly Journal of the Royal Meteorological Society, 146, 1999
Howard A. W. et al., 2012, ApJS, 201, 15
Irwin J., Berta Z. K., Burke C. J., Charbonneau D., Nutzman P., West A. A., Falco E. E., 2011, ApJ, 727, L56
Jansen T., Scharf C., Way M., Del Genio A., 2019, ApJ, 875, L79
Jernigan J., Laflèche É., Burke A., Olson S., 2023, ApJ, 944, L205
Kaib N. A., Raymond S. N., 2024, ApJ, 962, L28
Kane S. R., Gelino D. M., 2012, Astrobiology, 12, 940

Kane S. R., Li Z., Wolf E. T., Ostberg C., Hill M. L., 2021, AJ, 161, 31
Kasting J. F., 1991, Icarus, 94, 1
Kasting J. F., Whitmire D. P., Reynolds R. T., 1993, Icarus, 101, 108
Kay C., Opher M., Kornbleuth M., 2016, ApJ, 826, L195
Kopparapu R. K. et al., 2013, ApJ, 765, L131
Lachaume R., Dominik C., Lanz T., Habing H. J., 1999, A&A, 348, 897
Lammer H. et al., 2007, Astrobiology, 7, 185
Linsenmeier M., Pascale S., Lucarini V., 2015, Planet. Space Sci., 105, 43
Lovelock J. E., 1965, Nature, 207, 568
Luger R., Barnes R., Lopez E., Fortney J., Jackson B., Meadows V., 2015, Astrobiology, 15, 57
Malik M., Kitzmann D., Mendonça J. M., Grimm S. L., Marleau G.-D., Linder E. F., Tsai S.-M., Heng K., 2019, AJ, 157, 170
Mamajek E. E., Hillenbrand L. A., 2008, ApJ, 687, L1264
Marvin C. J., Reiners A., Anglada-Escudé G., Jeffers S. V., Boro Saikia S., 2023, A&A, 671, 162
McKay C. P., 2014, Proceedings of the National Academy of Science, 111, 12628
McLaughlin D. B., 1924, ApJ, 60, L22
Meadows V. S., Barnes R. K., 2018, in Deeg H. J., Belmonte J., eds, Factors Affecting Exoplanet Habitability. Springer International Publishing AG, Berlin, Germany, p. 2771
Mlawer E. J., Payne V. H., Moncet J. L., Delamere J. S., Alvarado M. J., Tobin D. C., 2012, Philosophical Transactions of the Royal Society of London Series A, 370, 2520
Modi A., Estrela R., Valio A., 2023, MNRAS, 525, 5168
Murante G. et al., 2020, MNRAS, 492, 2638
Murray C. D., Dermott S. F., 1999, Solar system dynamics. Cambridge Univ. Press, Cambridge
Nikolov N., Sainsbury-Martinez F., 2015, ApJ, 808, L57
North G. R., Coakley J. A. J., 1979, Journal of the Atmospheric Sciences, 36, 1189
North G. R., Short D. A., Mengel J. G., 1983, J. Geophys. Res., 88, 6576
Olson S. L., Schwieterman E. W., Reinhard C. T., Ridgwell A., Kane S. R., Meadows V. S., Lyons T. W., 2018, ApJ, 858, L14
Olson S. L., Jansen M., Abbot D. S., 2020, ApJ, 895, L19
Peale S. J., 1977, in Burns J. A., ed., IAU Colloq. 28: Planetary Satellites, Rotation Histories of the Natural Satellites. University of Arizona Press, Tucson, AZ, p. 87
Perrin M. Y., Hartmann J. M., 1989, J. Quant. Spec. Radiat. Transf., 42, 311
Powner M. W., Gerland B., Sutherland J. D., 2009, Nature, 459, 239
Ramirez R. M., Kaltenegger L., 2018, ApJ, 858, L72
Rauer H. et al., 2014, Exp. Astron., 38, 249
Ricker G. R., Winn J. N., Vanderspek R., 2015, J. Astron. Telesc. Instrum. Syst., 1, 014003
Rimmer P. B., Xu J., Thompson S. J., Gillen E., Sutherland J. D., Queloz D., 2018, Science Advances, 4, eaar3302
Rossiter R. A., 1924, ApJ, 60, L15
Sagan C., 1973, Journal of Theoretical Biology, 39, 195
Sagan C., Chyba C., 1997, Science, 276, 1217
Sancho L. G., de la Torre R., Horneck G., Ascaso C., de los Rios A., Pintado A., Wierzchos J., Schuster M., 2007, Astrobiology, 7, 443
Sanz-Forcada J., Ribas I., Micela G., Pollock A. M. T., García-Álvarez D., Solano E., Eiroa C., 2010, A&A, 511, 8
Shields A. L., Meadows V. S., Bitz C. M., Pierrehumbert R. T., Joshi M. M., Robinson T. D., 2013, Astrobiology, 13, 715
Shields A. L., Ballard S., Johnson J. A., 2016, Phys. Rep., 663, 1
Silva L., Vladilo G., Murante G., Provenzale A., 2017, MNRAS, 470, 2270
Simon A. E., Szabó G. M., Szatmáry K., Kiss L. L., 2010, MNRAS, 406, 2038
Simonetti P., Vladilo G., Silva L., Maris M., Ivanovski S. L., Biasiotti L., Malik M., von Hardenberg J., 2022, ApJ, 925, L105
Simonetti P. et al., 2024, ApJ, 960, L27
Sneep M., Ubachs W., 2005, J. Quant. Spec. Radiat. Transf., 92, 293
Soderblom D. R., Duncan D. K., Johnson D. R. H., 1991, ApJ, 375, L722
Spiegel D. S., Menou K., Scharf C. A., 2008, ApJ, 681, L1609
Spiegel D. S., Raymond S. N., Dressing C. D., Scharf C. A., Mitchell J. L., 2010, ApJ, 721, L1308
Spinelli R., Borsa F., Ghirlanda G., Ghisellini G., Haardt F., 2023, MNRAS, 522, 1411
Stamenković V., Noack L., Breuer D., Spohn T., 2012, ApJ, 748, L41
Stassun K. G. et al., 2019, AJ, 158, 138
Stevens D. J., Gaudi B. S., 2013, PASP, 125, 933
Stevenson D. J., 2010, Space Sci. Rev., 152, 651
Suárez Mascareño A., Rebolo R., González Hernández J. I., Esposito M., 2015, MNRAS, 452, 2745
Tachinami C., Senshu H., Ida S., 2011, ApJ, 726, L70
Tobie G., Grasset O., Dumoulin C., Mocquet A., 2019, A&A, 630, 70
Trainer M. G., Pavlov A. A., Dewitt H. L., Jimenez J. L., McKay C. P., Toon O. B., Tolbert M. A., 2006, Proceedings of the National Academy of Science, 103, 18035
Turnbull M. C., 2015, preprint (arXiv:1510.01731)
Valencia D., O'Connell R. J., Sasselov D., 2006, Icarus, 181, 545
Vidotto A. A., Jardine M., Morin J., Donati J. F., Lang P., Russell A. J. B., 2013, A&A, 557, 67
Vladilo G., Murante G., Silva L., Provenzale A., Ferri G., Ragazzini G., 2013, ApJ, 767, L65
Vladilo G., Silva L., Murante G., Filippi L., Provenzale A., 2015, ApJ, 804, L50
Wagner W., Kretzschmar H.-J., 2008, International Steam Tables – Properties of Water and Steam based on the Industrial Formulation IAPWS-IF97. Springer Berlin Heidelberg, Berlin, Heidelberg, p. 7
Walker J. C. G., Hays P. B., Kasting J. F., 1981, J. Geophys. Res., 86, 9776
Wang Y., Liu Y., Tian F., Hu Y., Huang Y., 2017, preprint (arXiv:1710.01405)
Way M. J., Georgakarakos N., 2017, ApJ, 835, L1
West A. A., Hawley S. L., Bochanski J. J., Covey K. R., Reid I. N., Dhital S., Hilton E. J., Masuda M., 2008, AJ, 135, 785
Williams D. M., Kasting J. F., 1997, Icarus, 129, 254
Williams D. M., Pollard D., 2002, in Montesinos B., Gimenez A., Guinan E. F., eds, ASP Proc. Conf. Vol. 269, The Evolving Sun and its Influence on Planetary Environments. Astron. Soc. Pac., San Francisco, p. 201
Williams D. M., Pollard D., 2003, International Journal of Astrobiology, 2, 1
Wordsworth R., Kalugina Y., Lokshtanov S., Vigasin A., Ehlmann B., Head J., Sanders C., Wang H., 2017, Geophys. Res. Lett., 44, 665
Zhuang Q., Gao X., Yu Q., 2012, ApJ, 758, L111
Zsom A., Seager S., de Wit J., Stamenković V., 2013, ApJ, 778, L109
Zuluaga J. I., Cuartas P. A., 2012, Icarus, 217, 88

This paper has been typeset from a TEX/LATEX file prepared by the author.